Chapter 7
Application of Mössbauer Spectroscopy to Li-Ion and Na-Ion Batteries

Pierre-Emmanuel Lippens

Abstract Electrochemical energy storage is essential in everyday life and is crucial for energy transition requiring sustainable energy sources and clean transportation. Li-ion batteries are widely used due to their high energy density while other technologies are now emerging, as Na-ion batteries, to offer a variety of energy storage systems. The electrode materials are one of the key components that should be improved for better battery performance. This requires the investigation of the electrochemical reactions that take place within the batteries. Mössbauer spectroscopy is a powerful tool to probe the local environment at the atomic scale in electrode materials. This technique can be used for ex situ analyses or to follow in situ the electrochemical reactions. In this chapter, some general aspects of currently commercialized Li-ion batteries are briefly described to introduce electrode materials, electrochemical mechanisms and their characterizations. The basic concepts of the Mössbauer effect and hyperfine interactions are presented to define the Mössbauer parameters that provide information about structural, electronic and magnetic properties, with a special attention to in situ measurements. Then, some selected examples of insertion, alloying and conversion materials are considered to illustrate the application of ^{57}Fe and ^{119}Sn Mössbauer spectroscopies to elucidate reaction mechanisms in Li-ion and Na-ion batteries.

7.1 Introduction

In 2019, the Nobel Prize in Chemistry was awarded to John B. Goodenough, M. Stanley Whittingham and Akira Yoshino for their contributions to the development of Li-ion batteries. Li-ion batteries are now used in a wide range of applications from small electronic devices to large storage systems for sustainable and renewable energy sources, including electric transportation [1–4]. This technology has already changed the life of many people worldwide and is certainly a key element for energy

P.-E. Lippens (✉)
Institut Charles Gerhardt, UMR 5253 CNRS Université de Montpellier, Place Eugène Bataillon, 34095 Montpellier Cedex 5, France
e-mail: pierre-emmanuel.lippens@umontpellier.fr

© Springer Nature Singapore Pte Ltd. 2021

Y. Yoshida and G. Langouche (eds.), *Modern Mössbauer Spectroscopy*,
Topics in Applied Physics 137, https://doi.org/10.1007/978-981-15-9422-9_7

transition. The success of Li-ion batteries is mainly due to their high energy density, arising from the low atomic mass of lithium and its high electropositivity that give high electrode capacity and high cell voltage, respectively. But such lightweight, rechargeable and powerful batteries are also the result of a long series of fundamental research and technology advances [5].

The early use of lithium metal as negative electrode for lithium batteries encountered severe safety issues due to Li dendritic growth, leading to internal short-circuits [6]. In a Li-ion battery, the negative electrode is usually made from an intercalation material like graphite, while Li^+ ions are provided by the positive electrode mostly comprising a layered lithium transition metal oxide. The Li^+ ions move between the two electrodes through an electrolyte that usually consists of a lithium salt and a liquid organic solvent, although solid electrolytes should be a promising alternative to enhance safety and energy density [7–9].

Depending on their applications, Li-ion batteries should have high power and/or high energy density, but in all cases they should be safe, with long calendar and cycle life, environmentally friendly, and as cheap as possible. Everyone would like to use small and light batteries that can be charged fast and do not explode! The performance of conventional Li-ion batteries based on the "negative electrode-liquid electrolyte-positive electrode" configuration depends on the properties of each component and on their combination. It is a real challenge to improve significantly such complex systems, which not only requires to optimize the electrode materials and electrolyte, but also the interfaces, the design of electrodes and cells, the current collectors, etc. [10–16]. Such a task needs a multidisciplinary approach combining different fields of chemistry and physics, but above all, the application of different techniques of characterization [17–23].

Mössbauer spectroscopy can be used in different ways to improve the performance of Li-ion batteries [24–27]. The most obvious application concerns the characterization of the structural and electronic properties of pristine electrode materials, following the methodologies developed in solid-state chemistry. The technique provides a lot of information about the local environment of atoms through electric and magnetic interactions. Mössbauer spectroscopy is also of high interest for the characterization of poorly crystalline materials, amorphous phases and nanoparticles since X-ray diffraction cannot be used due to the loss of long-range order. This aspect is not only important for pristine electrode materials but also for the products of electrochemical reactions that can be, under certain experimental conditions, studied ex situ, i.e. by extracting the electrode material out of the electrochemical cell at a certain stage of lithiation or sodiation.

Most importantly, Mössbauer spectroscopy is a powerful technique to investigate reaction mechanisms under operating conditions as shown, for example, in catalysis [28]. By considering specific electrochemical cells that make γ-ray transmission possible, the technique can be used for in situ or operando studies of electrochemical reactions. Although these two terms are often used indistinctly in the literature, one can consider that operando measurements refer to batteries in charge or discharge operations while in situ characterizations concern all studies where batteries are not

disassembled. In situ Mössbauer spectroscopy is of high interest for the characterization of lithiated and sodiated materials that are often air and moisture sensitive, but also and above all, this technique provides information about the reactions taking place in electrochemical cells. It should be noted that such reactions depend on the experimental conditions such as the current imposed to the cell in galvanostatic regime. While a high current usually enhances kinetic effects, a low current should be used to approach thermodynamic equilibrium. This means that the experimental protocol used for in situ measurements should be carefully defined. Finally, it is worth noting that in situ experiments are not always needed to investigate reaction mechanisms as shown in Sect. 7.6.4.

There are some restrictions in the application of Mössbauer spectroscopy to Li-ion and Na-ion batteries. The number of isotopes that can be used with a conventional in-lab Mössbauer technique (*vs.* synchrotron radiation-based Mössbauer spectroscopy) is limited. Fortunately, many positive and negative electrode materials contain iron and tin atoms, respectively, that are the most studied elements by Mössbauer spectroscopy. Both ^{57}Fe and ^{119}Sn isotopes can be considered for room temperature investigations of Li-ion or Na-ion batteries. Other isotopes have been used such as ^{121}Sb [29] or ^{99}Ru [30] but these studies mainly focused on the characterization of pristine electrode materials or ex situ measurements due to the required specific experimental conditions. For electrode materials that do not contain any Mössbauer isotopes, doping with a Mössbauer probe was also used as reported for Sn doped TiO_2 [31] or Fe doped $Li_2Ti_3O_7$ [32].

This chapter primarily deals with the application of Mössbauer spectroscopy to investigate electrochemical mechanisms in Li-ion and Na-ion batteries. This means that the characterization of pristine electrode materials is not really considered here although it is an important task for the optimization of these materials. However, this aspect is similar to the well-documented applications of Mössbauer spectroscopy in materials science and the methodology is not different for electrode materials. Since this book is addressed to a large audience, some aspects of Li-ion batteries and Mössbauer spectroscopy are first introduced to give the basic knowledge and the key parameters for elucidating the electrochemical mechanisms in batteries.

This chapter covers general and specific aspects of Li-ion batteries and Mössbauer spectroscopy. The main features of Li-ion batteries are given in Sect. 7.2, including a presentation of the most commonly used electrode materials, the main types of electrochemical reactions and some methods of characterization. Section 7.3 deals with basic considerations on Mössbauer spectroscopy and is focused on electric and magnetic hyperfine interactions that are at the origin of the Mössbauer parameters. Some specific aspects of in situ Mössbauer measurements are also given. Finally, the application of Mössbauer spectroscopy to the study of electrochemical reactions in Li-ion and Na-ion batteries are illustrated by selected examples of insertion reactions in Sect. 7.4, alloying reactions in Sect. 7.5 and conversion reactions in Sect. 7.6.

7.2 Electrochemical Energy Storage

7.2.1 Li-Ion Batteries

A Li-ion battery is composed of one or several electrochemical cells that are connected in parallel and/or in series to increase the current and/or the voltage, respectively. For instance, the Li-ion battery pack of the Toyota Prius Plug-in hybrid cars consists of 5 battery stacks, each containing 19 cells for a total energy of 8.8 kW h and a voltage of 352 V. There are different types of commercialized electrochemical cells, including cylindrical, prismatic, pouch and coin cells [33]. A typical Li-ion electrochemical cell is formed by a positive electrode, a negative electrode, a separator to avoid electrical contacts between the electrodes and an electrolyte for internal ionic charge transfer. Each electrode consists of a metallic film, copper for the negative electrode and aluminum for the positive electrode, connected to an external cell terminal and coated (single or double side) by a polymer film containing the electrochemically active particles and electronic conductive additives. In cylindrical and prismatic cells, the two electrodes and the separator are coiled, providing higher surface areas and storage capacities (Fig. 7.1).

During the charge of a Li-ion cell, the energy provided by a power source connected to the cell generates a current of electrons that flows from the positive to the negative electrode in the external circuit. This produces a movement of Li^+ ions through the electrolyte within the cell in the same direction (Fig. 7.2). Thus, the first charge of the cell requires that the positive electrode material contains and provides to the negative electrode the Li^+ ions. During the discharge, the electrons and Li^+ ions move from the negative to the positive electrode in the external circuit and in the cell, respectively.

The first lithium batteries were affected by serious problems due to the combined use of pure lithium metal as negative electrode and solvent-based organic electrolytes. The reaction of metallic lithium with liquid electrolyte leads to the progressive growth of Li dendrites at the surface of the negative electrode towards the positive electrode at each charge-discharge cycle, ending with internal electrical short-circuits [6, 9].

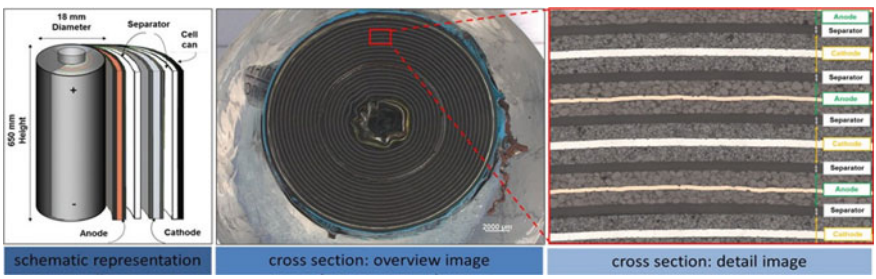

Fig. 7.1 Schematic view of a cylindrical Li-ion cell and cross section images showing coiled negative (anode) and positive (cathode) electrodes with separator. Copyright: ©ZEISS Microscopy

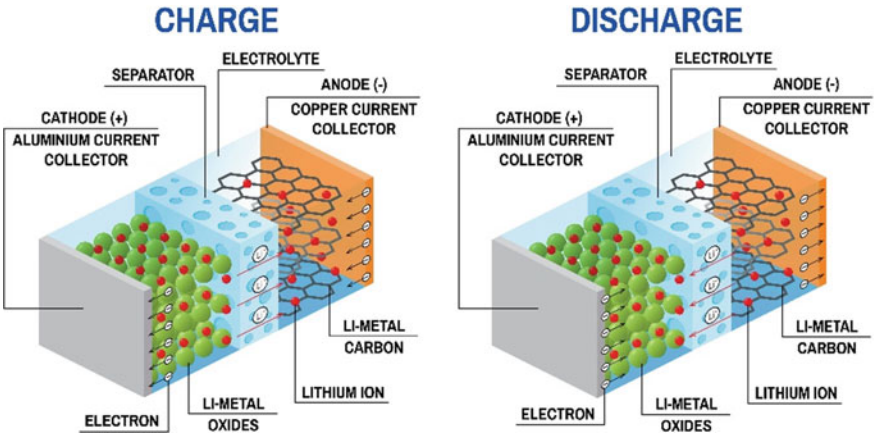

Fig. 7.2 Schematic view of a Li-ion cell showing that Li^+ ions and electrons move from the positive (cathode) to the negative (anode) electrode during the charge and back when discharging. The Li^+ ions move in the cell through the electrolyte and the electrons in the external circuit. The separator prevents electrical contacts between electrodes

To avoid lithium electrodeposition and resolve safety issues, metallic lithium was replaced by an intercalation material and combined with a positive electrode material as a source of lithium. The first Li-ion batteries, commercialized by Sony in 1991, were made up of carbon and $LiCoO_2$ as negative and positive electrode materials, respectively. Since then, many works have been devoted to electrode materials and electrolytes to improve the performance of Li-ion batteries including energy density, rate capability, lifespan and safety. The energy density of an electrochemical cell can be enhanced by increasing the electrode capacity and the cell voltage. In order to increase the cell voltage, much effort has been expended to increase the potential of the positive electrode since the potential of the commonly used carbonaceous negative electrodes is close to that of metallic lithium and cannot be decreased further. For both positive and negative electrode materials, the capacity, but also the rate capability and the cycle life should be improved for better battery performance.

Most of the commercialized positive electrode materials are currently lithium transition metal oxides and phosphates. Layered compounds $LiMO_2$, where M = Co, Mn, Ni or mixtures thereof, are often used due to their high potential versus Li/Li^+ and their high specific capacity. However, there are some issues with the stability of layered compounds and the use of Co in the composition of electrode materials. This metal is expensive and cobalt mining has bad environmental and social consequences. A lot of works have been devoted to decrease the cobalt content or replace layered metal oxides by other types of metal oxides such as spinel LiM_2O_4. Transition metal phosphates, such as olivine $LFePO_4$, are also an interesting alternative to $LiMO_2$. $LFePO_4$ based electrodes offer good cycle life, high specific power and safety but have lower operating potential and specific capacity than layered metal oxides.

The negative electrodes of Li-ion batteries are mainly based on carbon. Graphite can intercalate Li^+ ions, has a low cost and can be easily found or produced. Graphite can intercalate between the carbon layers up to 1 Li per 6 C, leading to specific and volumetric capacities of 372 mA h g^{-1} and ~800 mA h cm^{-3}, respectively. The voltage profile of a graphite based electrode, i.e., the electrode potential vs. Li/Li^+ as a function of the number of inserted Li, shows well-defined plateaus and a good reversibility. The mechanism is more complex for disordered forms of carbon such as hard carbons, soft unorganized carbons or natural graphite that contain a lot of defects, leading to different voltage profiles and electrode performances [34–36]. One issue with carbon is the possible formation of lithium dendrites under certain conditions due to its operating potential close to that of metallic lithium. In addition, specific and volumetric capacities should be increased. This is obtained by the addition of a small amount of silicon since this element has a specific capacity about ten times higher than carbon, but the increase of capacity is still too low for future applications.

Titanates (TiO_2, $Li_4Ti_5O_{12}$) have been commercialized as negative electrode materials for high power batteries. The high operating potential of titanate based electrodes provides a high level of safety but a lower energy density than carbon. Finally, other families of materials with higher operating potentials and capacities than carbon have been proposed but encountered different critical issues. For example, tin based materials were previously regarded as negative electrode materials for high energy density batteries with the trade names STALION by Fuji in 1997 [37] and NEXELION by Sony in 2005 [38]. Tin is of particular interest within the framework of this chapter since it is involved in different electrochemical mechanisms that can be studied by ^{119}Sn Mössbauer spectroscopy as shown in Sects. 7.5 and 7.6.

7.2.2 Electrochemical Mechanisms

Three main types of electrochemical reactions that take place in electrode materials are usually distinguished: insertion, alloying and conversion reactions.

Insertion or intercalation reactions: Li^+ ions are intercalated between layers (graphite, $LiMO_2$) or inserted into diffusion channels (Nasicon, $LiFePO_4$, $Li_4Ti_5O_{12}$) of a host material to form a solid solution without strong structural changes or a new phase (two-phase reaction). In the first case, the voltage profile has a typical S-shape whereas a two-phase reaction often shows a voltage plateau reflecting first-order phase transition. These reactions are often highly reversible.

Alloying reactions: Li atoms form chemical bonds with an element A (Si, Sn, etc.) leading to Li_xA alloys or compounds. Such reactions come along with strong volume variations, causing mechanical and chemical instabilities of the electrode. The formed species are often nanoparticles but they can coalesce during cycling. The generally observed staircase voltage profile reflects the succession of two-phase alloying reactions but kinetic limitations or the formation of metastable phases often smooth the voltage curve. These reactions are reversible but reducing the effect of volume variations is still a challenge for long-term cycling.

Conversion reactions: Li atoms react with AB (intermetallics, oxides, sulfides, etc.) to give A and Li_xB nanoparticles that usually form a composite. For example, the lithiation of SnO produces Sn and Li_2O nanoparticles. Conversion reactions can be reversible, irreversible and partially reversible as observed for transition metal oxides, tin intermetallics and tin oxides, respectively. The voltage profile is formed by two plateaus for lithiation and delithiation, respectively, showing a large voltage polarization. Some conversion reactions are followed by alloying reactions.

It should be noted that the number of Li (or Na) per electrochemically active element involved in alloying and conversion reactions is generally higher than for insertion reactions, leading to high capacity electrode materials.

7.2.3 Characterization of Electrochemical Reactions

In Li-ion batteries using a lithium salt and organic solvent as electrolyte, the electrodes consist of metallic foils as current collectors that are coated with a film of several tens to hundreds micrometers obtained from a slurry containing powdered electrochemically active materials, electronic conductive additives and binder. All these components should be optimized for better performance. For instance, the electrode formulation is essential to form a mechanically and chemically stable composite film containing the active particles with electron and lithium conductive pathways. Concerning the electrochemically active materials, not only their intrinsic properties should be improved, but also their interfaces with the electrolyte and the other components of the film. Thus, the characterization of pristine electrode materials, as obtained after synthesis, should be combined with the analysis of the changes in these materials during charge-discharge cycles.

A lot of techniques used in solid-state chemistry and electrochemistry can be considered for the characterization of electrode materials and reaction mechanisms at different length and time scales. Electrode performance, such as volumetric and specific capacities, operating voltage, cycling and rate capabilities, and cycle life, can be evaluated from the measurements of the cell voltage or the electric current with different experimental protocols based on galvanostatic (constant current) or potentiostatic (constant voltage) regimes. Electrochemical experiments also provide useful information about the reactions taking place in the cell from the voltage profile, current or voltage relaxations, impedance, etc. For such experiments, but also for in situ characterizations, Li half-cells are used instead of Li-ion full-cells. In a Li half-cell, the negative electrode is lithium metal that should be considered as the reservoir of lithium while the positive electrode contains the active material under study. The latter material can be the positive or negative electrode material in a Li-ion full-cell. Thus, the discharge and charge of a Li half-cell correspond to the lithiation and delithiation of the electrode material under study, respectively, while the situation is somewhat more ambiguous for a Li-ion full-cell that contains the two types of electrodes. To avoid confusion, the terms lithiation and delithiation (sodiation and desodiation) are used along this chapter instead of charge and discharge, respectively.

One of the most commonly used techniques for studying electrode materials is X-ray diffraction (XRD). XRD has often been considered for the characterization of crystalline pristine materials and their evolution during the lithiation-delithiation cycles. This is of particular interest to follow changes in the lattice parameters and atomic positions of crystalline insertion materials, resulting from the insertion of ions, or to identify new formed crystalline phases. However, this technique fails for poorly crystalline, nanosized and amorphous phases as often encountered in pristine electrode materials or detected as products of alloying and conversion reactions. Such characterizations require local probe techniques, including X-ray photoelectron spectroscopy (XPS), which is a surface sensitive technique, X-ray absorption spectroscopy (XAS), nuclear magnetic resonance (NMR), electron paramagnetic resonance (EPR) or Mössbauer spectroscopy. These techniques not only give information about the local environment of the probe elements, but also on the electronic, magnetic and dynamic properties of the electrode materials. For instance, they are used to determine the oxidation and spin states, charge anisotropy and bond properties of atoms in the electrode particles, but they are also used to identify the products formed during insertion-deinsertion processes within the electrode and at the interface with the electrolyte. All these techniques go along with imaging techniques, such as transmission electron microscopy (TEM), scanning electron microscopy (SEM) or atomic force microscopy (AFM), that provide direct visualized information about changes in the size, morphology and aggregation of the electrode particles caused by electrochemical reactions.

7.3 Basic Aspects of Mössbauer Spectroscopy

7.3.1 The Mössbauer Effect

The Mössbauer effect is briefly described here, while more details can be found in many textbooks [39–42]. This effect is based on transitions between excited and ground nuclear states at energy E_γ (~keV). An excited free nucleus can reach equilibrium by emitting a γ-photon (γ decay) of energy $E_\gamma - E_R$, where E_R (~meV) is the nuclear recoil energy, while a nucleus of the same isotope can be excited by absorbing a γ-photon of energy $E_\gamma + E_R$. The energy distribution of γ-rays is a Lorentzian curve whose the linewidth Γ (~neV) is related to the mean lifetime of the nuclear excited state by the Heisenberg uncertainty principle. The perfect overlap of the emission and absorption Lorentzian curves (resonance) is not possible for free or weakly bound atoms because the nuclear recoil energy is several orders of magnitude higher than Γ. However, R.L. Mössbauer observed such a resonance in solids that can be explained as follows. In a solid, the recoil energy of nuclei during the emission of γ-rays should be transferred to the lattice, but the quantization of atomic vibrations requires that such transfer is only possible for energy values corresponding to the creation of phonons. Thus, a fraction of the excited nuclei can emit γ-photons without

energy transfer to the lattice (zero-phonon transition), i.e. with a Lorentzian energy distribution centered at E_γ. Conversely, a fraction of the nuclei at ground state in a solid can absorb γ-photons without recoil, i.e., at the same energies as the source of γ-rays and, therefore, resonance is possible. This fraction of nuclei, f, also known as the recoil-free fraction, corresponds to the probability of recoil-free emission or absorption of γ-rays. The recoil-free fraction is a fundamental quantity, not only to explain the Mössbauer effect, but also for the applications of Mössbauer spectroscopy since f depends on the γ-ray energy and the lattice dynamical properties. To summarize, the Mössbauer effect can be defined as the resonant and recoil-free emission or absorption of γ-rays by a fraction of the nuclei of atoms bound in a solid. In this chapter, these atoms are called the "Mössbauer atoms".

Although changes in the energy of nuclear states due to interactions with the surrounding electrons and atoms are weak (~neV), the extremely small linewidth Γ prevents resonance except if both source and absorber of γ-rays are identical materials. However, R.L. Mössbauer proposed to use the Doppler effect to modulate the energy of γ-rays by small movements of the source relative to the absorber, making possible the detection of the Mössbauer effect in any absorbing samples containing the same Mössbauer isotope as the source. Thus, a conventional in-lab Mössbauer spectroscopy in transmission geometry consists basically of a radioactive source with a drive system, an absorber which is the sample under investigation and a γ-ray detector. The relation between the velocity of the source relative to the absorber, v, and the energy shift, E, is given by the relation

$$v = \frac{c}{E_\gamma} E \tag{7.1}$$

where c is the light velocity. For the 1/2−3/2 nuclear transition in ^{57}Fe (E_γ = 14.4 keV) and ^{119}Sn (E_γ = 23.9 keV), v = 1 mm s^{-1} corresponds to energy shifts of 4.8 10^{-8} eV and 8.0 10^{-8} eV, respectively. This velocity can be compared to the natural linewidths of ^{57}Fe (Γ = 0.1 mm s^{-1}) and ^{119}Sn (Γ = 0.32 mm s^{-1}) and is typical of nuclear energy changes for these two isotopes, leading to velocity ranges for ^{57}Fe and ^{119}Sn Mössbauer spectra usually less than ±10 mm s^{-1}. The high intrinsic energy resolution ($\Gamma/E_\gamma \sim 10^{-12}$) is really the most remarkable feature of Mössbauer spectroscopy, making possible the detection of very weak changes in nuclear transition energy arising from electric and magnetic interactions with the surrounding charges. These interactions are localized within the nucleus of the Mössbauer atoms that should be regarded as atomic probes. The use of such local probes is of high interest for electrode materials. For instance, Li can randomly occupy the vacant sites of an insertion material and modify the electronic configuration of the Mössbauer atoms, leading to changes in oxidation state or causing structural relaxation. For alloying and conversion reactions, the electrochemically formed species are usually nanosized and disordered, so they can be more easily identified by Mössbauer spectroscopy than XRD.

The standard application of in-lab Mössbauer spectroscopy is restricted to a small number of isotopes. ^{57}Fe and ^{119}Sn are by far the most commonly used isotopes, but others like ^{121}Sb [29] or ^{99}Ru [30] have also been considered to study electrode materials. For other chemical elements, synchrotron radiation based Mössbauer spectroscopy [43] or atomic substitution with a Mössbauer isotope should be envisaged. In some cases, the low concentration of Mössbauer atoms requires long-term experiments that are not always compatible with operando measurements.

Information about samples under investigation are mainly obtained from the analysis of the shape of the Mössbauer spectra that are usually not a single Lorentzian line (see Sect. 7.3.6). Electric and magnetic interactions between the Mössbauer nuclei and their local environment lead to the shift and splitting of the nuclear states, which affects the number and energy of the recoil-free nuclear transitions. These interactions are at the origin of three main Mössbauer parameters that can be, in principle, obtained from the Mössbauer spectra: isomer shift, quadrupole splitting and hyperfine magnetic field. These parameters and the recoil-free fraction are described in the following subsections.

7.3.2 Isomer Shift

The hyperfine interactions between the nuclear charge density and the Coulomb potential due to the electron density are localized within the nucleus. The atomic nucleus has a small and finite size and can be non-spherical, leading to monopole and quadrupole electric interactions that are related to the average size of the nucleus considered as a sphere and the deviation from the non-spherical shape of the nucleus, respectively. The monopole and quadrupole interactions are at the origin of the isomer shift and quadrupole splitting, respectively. For the determination of the isomer shift, it is first necessary to evaluate the change in the nuclear energy level, E, due to the Coulomb interaction between the charge Ze of the nucleus, where Z is the atomic number and e is the elementary charge, and the electron density at the nucleus, $\rho(0)$:

$$E = \frac{Ze^2\langle r_n^2\rangle}{6\varepsilon_0}\rho(0) \tag{7.2}$$

where ε_0 is the vacuum permittivity and $\langle r_n^2\rangle$ is the average value of the squared nuclear radius that depends on the nuclear spin number I. Thus, the monopole interaction leads to different values of E for the two nuclear spin states involved in a nuclear transition and the energy of this transition is modified by ΔE. For the nuclear transition 1/2–3/2 (^{57}Fe, ^{119}Sn), $\Delta E = E(I = 3/2) - E(I = 1/2)$ depends on the difference between the average values of the squared nuclear radii for the excited ($I = 3/2$) and ground ($I = 1/2$) nuclear states: $\Delta\langle r_n^2\rangle = \langle r_n^2(I = 3/2)\rangle - \langle r_n^2(I = 1/2)\rangle$. This difference is positive for ^{119}Sn and negative for ^{57}Fe. The Mössbauer atoms in the source and absorber have generally different local environments, leading to different

electronic densities at the nucleus, $\rho_s(0)$ (source) and $\rho_a(0)$ (absorber), and therefore, different energy transitions: ΔE_a and ΔE_s. The isomer shift is given by $\delta = \Delta E_a - \Delta E_s$, which corresponds to the energy shift of the resonance line relative to the source. The isomer shift is a relative quantity and the origin can be chosen arbitrary. A reference material is often considered instead of the source and $\rho_s(0)$ is replaced by $\rho_{ref}(0)$. This defines the zero-velocity of the isomer shift scale. In this chapter, the commonly used references α-Fe for ^{57}Fe and $BaSnO_3$ for ^{119}Sn are considered, but others can be found in the literature, which should be taken into account to compare the isomer shifts originating from different works. The expression of the isomer shift obtained from Eq. (7.2) is

$$\delta = \frac{Ze^2}{6\varepsilon_0}\Delta\langle r_n^2\rangle\big(\rho(0) - \rho_{ref}(0)\big) \tag{7.3}$$

Since $\Delta\langle r_n^2\rangle$ is constant for a given isotope, the following simplified expression is often used for chemical applications:

$$\delta = \alpha\big(\rho(0) - \rho_{ref}(0)\big) \tag{7.4}$$

where the constant α is positive for ^{119}Sn and negative for ^{57}Fe, leading to opposite variations of δ versus $\rho(0)$ for these two isotopes. The value of α can be evaluated from the correlation between the experimental values of δ and the theoretical values of $\rho(0)$ for a series of reference materials [44–49]. For example, the values of $\rho(0)$ were evaluated for a series of tin compounds with density functional theory (DFT), using the linearized augmented plane wave (LAPW) method [50]. A good $\delta-\rho(0)$ linear correlation is observed (Fig. 7.3) as expected from Eq. (7.4). The calibration constant α obtained by linear regression for this series of compounds can then be used with $\rho(0)$ calculated by the LAPW method and Eq. (7.4) to evaluate the theoretical values of δ for other tin based phases as illustrated in Sects. 7.5 and 7.6.

The isomer shift provides information about the local environment of a Mössbauer atom through the electron density at the nucleus. Many studies have been devoted to the interpretation of the isomer shift from the evaluation of $\rho(0)$ or from some more qualitative but very fruitful approaches [51–53]. For instance, it is possible to relate the variations of the isomer shift to the valence electron populations of the Mössbauer atoms. First, it is important to note that only the s electrons and some relativistic p electrons are inside the nucleus, and the main contributions to $\rho(0)$ come, in descending order, from 1s, 2s, 3s, etc. electrons. However, changes in p-type and d-type wavefunctions influence the s-type wavefunctions (shielding effect) even at the nucleus. Since most of the modifications in the local environment of the Mössbauer atoms affect the chemical bonds and the valence electron density, one can consider, as a first approximation, that the contribution of core electrons $\rho_c(0)$ is constant and $\rho(0)$ mainly changes with the valence electron contribution $\rho_v(0)$. As shown by atomic calculations, the latter term strongly increases with the number of s-type valence electrons and decreases, but to a lesser extent, with the number of

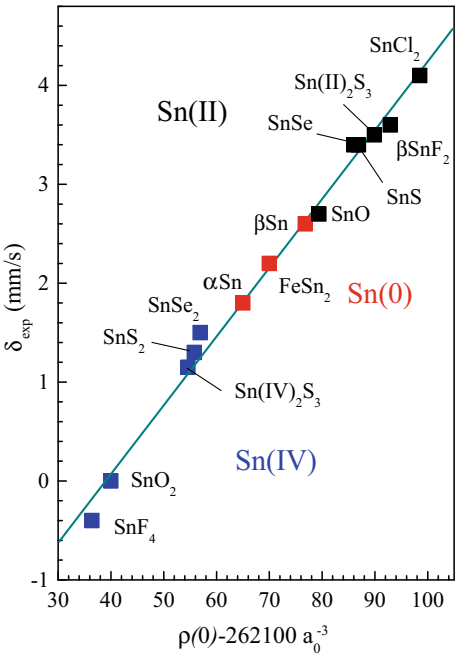

Fig. 7.3 Correlation between the experimental values of the ^{119}Sn isomer shift, δ_{exp}, relative to $BaSnO_3$ and the theoretical DFT-LAPW values of the electronic density at the nucleus $\rho(0)$. The values corresponding to Sn(IV), Sn(0) and Sn(II) compounds are shown in blue, red and black, respectively

p-type or d-type valence electrons. It is possible to derive an approximate analytical expression of $\rho_v(0)$ from the values obtained for different electron configurations of a free atom [51, 52]. A simple expression was derived for Sn and used for the tight-binding interpretation of the isomer shifts of tin chalcogenides [54]. This expression can be further simplified to qualitatively show the relative contributions of the Sn valence electrons

$$\rho_v(0) \sim N_{5s} - 0.1N_{5p} \tag{7.5}$$

where N_{5s} and N_{5p} are the Sn 5s and Sn 5p electron populations, respectively, obtained by integration of the local densities of occupied states within the tight-binding approximation. The oversimplified expression (7.5) should only be used to analyze some trends in the variations of the isomer shift and is just considered here to show that $\rho_v(0)$, and therefore δ, strongly increases for the series $N_{5s} = 0$–1–2 and, to a lesser extent, decreases with N_{5p}. This explains that the isomer shifts of Sn(IV), Sn(0) and Sn(II) compounds are found in three distinct ranges of values as shown in Fig. 7.3.

Interpretations based on Eq. (7.5) are rather qualitative but it is possible to relate some trends in the variations of δ in terms of oxidation state or chemical bond. A similar distinction can be made for ^{121}Sb but the isomer shift decreases for the sequence Sb(V)-Sb(0)-Sb(III) because of the negative sign of α. The situation is more complex for ^{57}Fe because there are overlaps between some ranges of isomer

shifts corresponding to different iron oxidation and spin states. Other Mössbauer parameters, such as the quadrupole splitting or the hyperfine magnetic field, should be considered to resolve any ambiguity.

The isomer shift depends on the valence electron configuration of the Mössbauer atom and can be used to investigate changes in the type of ligand, oxidation state, chemical bonding, coordination number and bond lengths arising from electrochemical reactions in Li-ion or Na-ion batteries. A common situation is the reversible change of Fe oxidation state in Fe^{2+} cathode materials such as $LiFePO_4$ following the reaction

$$LiFe^{2+}PO_4 = Fe^{3+}PO_4 + Li^+ + e^- \tag{7.6}$$

The values of the ^{57}Fe Mössbauer isomer shift relative to α-Fe at room temperature are very different for $LiFe^{2+}PO_4$ ($\delta = 1.2$ mm s^{-1}) and $Fe^{3+}PO_4$: ($\delta = 0.6$ mm s^{-1}). Equation (7.6) indicates that the delithiation of $LiFePO_4$ leads to the decrease of the Fe 3d electron population and, through the shielding effect, to the increase of $\rho(0)$. The negative sign of α in Eq. (7.4) for ^{57}Fe explains the observed decrease of the isomer shift from $LiFePO_4$ to $FePO_4$. In this example, the two Fe oxidation states can be easily distinguished by only considering the values of the isomer shift because ferrous and ferric ions in $LiFePO_4$ and $FePO_4$, respectively, have both high spin states. Another example is the reduction of Sn(IV) into Sn(0) during the first lithiation of SnO_2 following the conversion reaction

$$Sn(IV)O_2 + 4Li^+ + 4e^- \rightarrow \beta Sn(0) + 2Li_2O \tag{7.7}$$

The ^{119}Sn Mössbauer isomer shifts relative to $BaSnO_3$ of SnO_2 and βSn at room temperature are 0 mm s^{-1} and 2.55 mm s^{-1}, respectively. They can be easily distinguished by ^{119}Sn Mössbauer spectroscopy.

7.3.3 Quadrupole Splitting

The quadrupole splitting originates from the interaction between the nuclear quadrupole moment and the electric field gradient (EFG) at the nucleus created by the anisotropic charge distribution surrounding the nucleus. The nuclear quadrupole moment exists for a nuclear spin state $I > 1/2$ and measures the deviation of the nuclear charge distribution from spherical symmetry. Both the EFG and the nuclear quadrupole moment operator $\hat{Q}$ are second rank tensors and the Hamiltonian H_{QI} resulting from quadrupole interactions is expressed as the product of these two tensors. By considering the EFG principal axis system: X, Y, Z, the Hamiltonian can be written [55]

$$H_{QI} = \frac{eQV_{ZZ}}{4I(2I-1)}\left[3\hat{I}_Z^2 - I(I+1) + \eta\left(\hat{I}_X^2 - \hat{I}_Y^2\right)\right] \tag{7.8}$$

where Q is an average value obtained from $\hat{Q}$ and usually defined as the nuclear quadrupole moment, which depends on the nuclear spin value I, V_{ZZ} is the EFG component of highest absolute value in the principal axis system, $\hat{I}_X$, $\hat{I}_Y$ and $\hat{I}_Z$ are the nuclear spin operators and η is the asymmetry parameter defined by

$$\eta = \frac{V_{XX} - V_{YY}}{V_{ZZ}} \tag{7.9}$$

where V_{XX} and V_{YY} are the two other components of the EFG tensor in the principal axis system such that $|V_{XX}| \leq |V_{YY}| \leq |V_{ZZ}|$. It should be noted that $0 \leq \eta \leq 1$. The nuclear energy levels are obtained by the diagonalization of the H_{QI} matrix in the basis of the nuclear spin states $|I, m_I>$, where m_I is the nuclear magnetic quantum number.

For the first excited nuclear state of ^{57}Fe and ^{119}Sn ($I = 3/2$), H_{QI} can be diagonalized analytically, giving two twofold degenerated energy levels of opposite signs for the states $|3/2, \pm 1/2>$ and $|3/2, \pm 3/2>$, respectively, that are separated by the energy

$$\Delta = \frac{1}{2} e Q V_{ZZ} \left(1 + \frac{\eta^2}{3}\right)^{1/2} \tag{7.10}$$

called the quadrupole splitting. Thus, there are two possible nuclear transitions between the ground state ($I = 1/2$) and the first excited state ($I = 3/2$). The corresponding Mössbauer spectrum is formed by a doublet of two resonant lines whose separation is given by Δ. Equation (7.10) indicates that the quadrupole splitting is proportional to the nuclear quadrupole moment of the excited state ($I = 3/2$). Its value can be determined experimentally or from the linear correlation between the experimental values of Δ and the theoretical values of EFG for a series of crystalline phases [49, 56–58]. As an example, the experimental values of the quadrupole splitting are reported against the DFT-LAPW values of the electronic term $| V_{ZZ} | \left(1 + \frac{\eta^2}{3}\right)^{1/2}$ for a series of tin compounds (Fig. 7.4). The slope of the regression line gives $Q = 10.5$ fm^2 in agreement with the experimental value $Q = 10.9(8)$ fm^2 [59].

Both V_{ZZ} and η provide information about the anisotropic charge distribution around the nucleus. For the 1/2–3/2 nuclear transition, these two terms cannot be obtained independently from the experimental value of the quadrupole splitting as shown by Eq. (7.10). This is nevertheless possible with a conventional experimental setup and the application of an external magnetic field.

For other nuclear transitions, the quadrupole interactions are more complex, requiring the numerical diagonalization of H_{QI} given by Eq. (7.8) in the basis of the nuclear spin states. This is, for example, the case of the 5/2–7/2 nuclear transition of ^{121}Sb. The 5/2 nuclear ground state and the 7/2 nuclear excited state are split into three and four substates, respectively, leading to eight allowed transitions. In that case, the values of V_{ZZ} and η can be determined from the Mössbauer spectra, but there are often large uncertainties on the values of η [60].

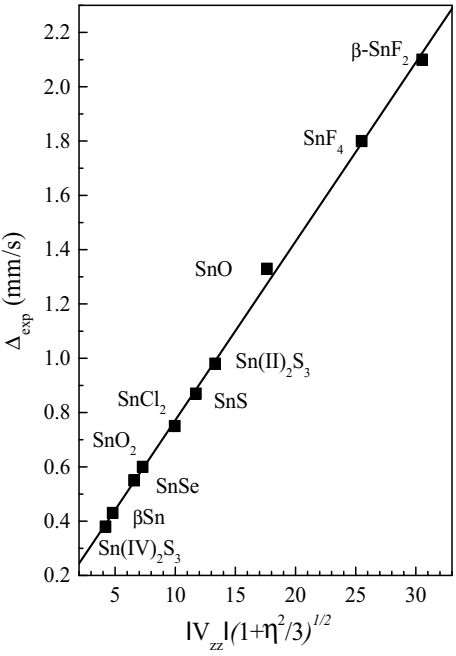

Fig. 7.4 Correlation between the experimental values of the ^{119}Sn quadrupole splitting, Δ_{exp}, and the theoretical DFT-LAPW values of the electronic term in Eq. (7.10)

Since $0 \leq \eta \leq 1$, η has often a small influence on Δ compared to V_{ZZ}, as shown by Eq. (7.10), and one can consider that the value of the quadrupole splitting is mainly given by V_{ZZ}. Different approaches have been used to interpret V_{ZZ}, including the point charge model that distinguishes between valence and lattice contributions [61]. However, the calculation of the EFG by quantum mechanical methods provides more accurate values and is often a better approach for a quantitative analysis [56].

Along the same line as the interpretation of the isomer shift described in Sect. 7.3.2, simple models were proposed to evaluate V_{ZZ} from the electron populations especially when the EFG originates from the valence electrons of the Mössbauer atom. For instance, the EFG at the Sn nucleus often arises from the Sn 5p electron anisotropy and, under certain assumptions, V_{ZZ} can be related to the Sn 5p electron asymmetry count ΔN_{5p}:

$$V_{ZZ} \sim \left\langle r^{-3} \right\rangle \Delta N_{5p} \tag{7.11}$$

with

$$\Delta N_{5p} = \frac{1}{2}\left(N_{5p_X} + N_{5p_Y}\right) - N_{5p_Z} \tag{7.12}$$

where $\left\langle r^{-3} \right\rangle$ is the expectation value of r^{-3} for the Sn 5p states, N_{5p_i} is the Sn $5p_i$ orbital occupancy (or partial number of Sn $5p_i$ electrons) along the principal axis

$i = X, Y, Z$. Equations (7.11) and (7.12) show that the sign of V_{ZZ} reflects the accumulation ($V_{ZZ} < 0$) or the depletion ($V_{ZZ} > 0$) of the Sn 5p electrons along the Z axis relative to the average number of the remaining Sn 5p electrons in the XY plane perpendicular to Z.

For the 1/2–3/2 nuclear transition, the sign of V_{ZZ} cannot be determined experimentally except for combined electric quadrupole and magnetic interactions. However, the magnitude of Δ is of particular interest since it provides information about the anisotropy of the charge density around the Mössbauer atom, which depends on the Sn local structure and chemical bonds. For battery applications, this parameter can be used for the analysis of structural relaxations induced by Li or Na insertion or for the characterization of electrochemically formed small and poorly crystallized particles in two-phase, alloying and conversion reactions. The quadrupole splitting can also help to understand differences between metastable and stable crystalline phases as described in Sect. 7.6.1 for Li_7Sn_2.

7.3.4 Magnetic Splitting

The interaction between the magnetic moment of the nucleus $\boldsymbol{\mu}$ and the magnetic field at the nucleus $\boldsymbol{B}$ is described by the Hamiltonian

$$H = -\boldsymbol{\mu}.\boldsymbol{B} \tag{7.13}$$

with

$$\boldsymbol{\mu} = g_I \mu_n \hat{\boldsymbol{I}} \tag{7.14}$$

where g_I is the nuclear g-factor that depends on the nuclear spin number I, μ_n is the nuclear magneton and $\hat{\boldsymbol{I}}$ is the nuclear spin operator. The nuclear energy levels are

$$E = -g_I \mu_n B m_I \tag{7.15}$$

where the nuclear magnetic quantum number m_I takes the $2I + 1$ values $-I$, $-I + 1$,…, $I–1$, I, leading to the splitting of the nuclear states into $2I + 1$ substates (nuclear Zeeman splitting). For ^{57}Fe and ^{119}Sn isotopes, the ground ($I = 1/2$) and excited ($I = 3/2$) states are split into two ($m_{I=1/2} = \pm 1/2$) and four ($m_{I=3/2} = \pm 1/2, \pm 3/2$) substates, respectively, leading to six allowed dipole transitions by considering the selection rules $\Delta m_I = 0, \pm 1$. In that case, the Mössbauer spectrum is a sextet formed by six resonant absorption lines with intensities depending on the magnetization and γ-ray directions. For polycrystalline samples, the relative intensities are in the ratio 3:2:1:1:2:3.

The effective magnetic field at the nucleus comes from external and internal (in the Mössbauer atom) magnetic fields. In the latter case, the magnetic field at the nucleus originates from the spin imbalance at the nucleus (Fermi contact), the interaction between nuclear and electronic orbital moments, and the dipolar interaction between nuclear and electron spin moments. For example, the hyperfine magnetic field of ^{57}Fe in α-Fe is mainly due to the Fermi contact term arising from the difference between spin-up and spin-down electron densities at the nucleus $\rho_{\uparrow}(0) - \rho_{\downarrow}(0)$. The spin densities at the nucleus $\rho_{\uparrow}(0)$ and $\rho_{\downarrow}(0)$ are due to s-type electrons that are affected by the shielding effects of Fe $3d_{\uparrow}$ and Fe $3d_{\downarrow}$ valence electrons, respectively. The intensity of the hyperfine magnetic field can be obtained from the energy difference between the two external lines of the Mössbauer spectrum corresponding to the two nuclear transitions between states $|I, m_I>: |1/2,-1/2> - |3/2, -3/2>$ and $|1/2,1/2> - |3/2,3/2>$. According to Eq. (7.15), the observed value of 10.6 mm s^{-1} gives a hyperfine magnetic field of 33 T.

Although, the magnetic properties of electrode materials are not of direct interest for applications in batteries, they provide additional information that can help in the characterization of materials (crystallinity, particle size) or reaction mechanisms. Finally, it should be noted that the electric quadrupole and hyperfine magnetic interactions are not only described by a number, as the isomer shift, but they both depend on direction (EFG axes, magnetic field direction). If these two interactions occur simultaneously, the Hamiltonian resulting from Eqs. (7.8) and (7.13) must be generally solved numerically. In that case, the shape of the Mössbauer spectrum is more complex than line splitting. An example of such Mössbauer spectrum is given for antiferromagnetic $FeSn_2$ in Sect. 7.6.1.

7.3.5 *Recoil-Free Fraction*

The recoil-free fraction, f, is the probability of recoilless emission (source) or absorption (absorber) of γ-rays and is given by

$$f = exp\left(-k^2\left\langle x^2\right\rangle\right) \tag{7.16}$$

where k is the γ-ray wavenumber and $\left\langle x^2\right\rangle$ is the mean-square amplitude of the nucleus vibrations in the direction of γ-rays. A significant Mössbauer effect requires a large recoil-free fraction, which is obtained with a low value of k, i.e. of the γ-ray energy, typically lower than 150 keV, and a small value of $\left\langle x^2\right\rangle$. The nucleus displacements depend on the phonon spectrum of the solid that usually shows complex dispersion and must be evaluated by computational methods. However, analytical expressions can be derived by considering the Debye model. In the Debye model, the density of phonon states is assumed to increase as ω^2 up to the Debye frequency $\omega_D = K_B\theta_D/\hbar$, where θ_D is the Debye temperature, K_B is the Boltzmann constant and $\hbar$ is the reduced Planck constant. Simple analytical expressions can be obtained for $T \ll \theta_D$

$$f = exp\left(-\frac{3E_R}{2K_B\theta_D}\right) \tag{7.17}$$

and for $T \gg \theta_D$

$$f = exp\left(-\frac{6E_R T}{K_B\theta_D^2}\right) \tag{7.18}$$

where E_R is the nuclear recoil energy. At low temperature, *f(T)* does not vary with temperature while it strongly decreases as T increases for high temperatures. The temperature dependence of f is of high interest to determine the Debye temperature but can also be used for the analysis of Mössbauer spectra since the intensity of the resonant absorption line depends on f. For instance, the recoil-free fraction of βSn is small at room temperature, $f(300\ \text{K}) \approx 0.04$, and strongly increases with decreasing temperature, $f(77\ \text{K}) \approx 0.45$ and $f(4\ \text{K}) \approx 0.72$, leading to a strong increase of the intensity of the corresponding resonant absorption line [62]. For tin based electrode materials, it is often difficult to detect at room temperature a small amount of βSn that coexists with other tin phases such as Li_xSn, Na_xSn or Sn intermetallics. The isomer shifts are all in the Sn(0) range and the recoil-free fractions of the tin compounds or alloys are higher than that of βSn. By decreasing the temperature, the contribution of βSn to the Mössbauer spectrum increases, making the quantitative analysis more accurate.

The recoil-free fraction decreases with decreasing Debye temperature as shown for low and high temperatures by Eqs. (7.17) and (7.18), respectively. The physical meaning of the Debye temperature is not discussed here and θ_D is just regarded as a characteristic quantity of a solid that can be related to lattice stiffness. At a given temperature, solids with very different θ_D have different recoil-free fractions, which can help in the analysis of Mössbauer spectra when different phases coexist in the same absorbing sample. For example, the recoil-free fraction of SnO_2 at room temperature, $f(300\ \text{K}) = 0.55$, is more than ten times higher than that of βSn, leading to strongly different resonance line intensities. These two phases can be easily distinguished by Mössbauer spectroscopy since the difference between their Mössbauer isomer shifts is of about 2.6 mm s^{-1}. Thus, a small amount of SnO_2, as encountered in the oxide layer of βSn for instance, can be detected. Another situation concerns the reactants and products of electrochemical reactions with very different recoil-free fractions that must be taken into account to quantitatively characterize the electrochemical mechanisms as shown for conversion reactions in Sect. 7.6.

Finally, it should be noted that in a solid the Mössbauer atoms have generally different local environments, i.e., different types of neighbors, bond distances and angles. The values of f depend on the bonding forces on the Mössbauer atoms and can be significantly different for strongly different environments. In addition, f can be angular dependent for anisotropic environments. The situation is even more complex for multiphase systems as often encountered in electrode materials. In most cases,

the values of f cannot be evaluated for each Mössbauer site and some simplifying approximations are made as discussed in the next subsection.

7.3.6 The Mössbauer Spectrum

In Mössbauer spectroscopy, the energy of the γ-rays emitted by the source is modified by using the Doppler effect. It is then possible to detect the Mössbauer effect in any absorbing samples containing the same Mössbauer isotope as the source. A low activity source produces γ-rays with energy distribution modulated by an electromechanical drive system. In transmission geometry, the γ-rays transmitted through the absorber are transformed into an electric signal by a detector. From this signal, the number of γ-photons is recorded as a function of the source velocity by an electronic system synchronized with the source motion, which is periodic and has usually a constant acceleration. One Mössbauer spectrum is recorded every half-period of the source motion and the spectra are accumulated during many cycles to improve the signal-to-noise ratio. The resulting spectrum not only reflects the Mössbauer effect in the absorber but also depends on the γ-ray energy distribution of the source, which is assumed to have a single Lorentzian line shape in the present chapter.

For an absorber containing Mössbauer atoms with a single environment, e.g., a single crystallographic site occupied by the Mössbauer atoms in a crystal, it is convenient to define the dimensionless effective thickness by $t_a = \sigma_0 f_a n_a$, where σ_0 is the absorption cross-section at resonance, f_a is the recoil-free fraction of the Mössbauer isotope in the absorber and n_a is the number of atoms of the Mössbauer isotope per unit area. Thus, $f_a n_a$ represents the concentration of Mössbauer atoms that resonantly absorb γ-rays. The concentration n_a is obtained from the concentration of atoms of the same element by considering the natural abundance, e.g. 2.2% for ^{57}Fe and 8.6% for ^{119}Sn. These small values indicate that some samples with a low concentration of Mössbauer atoms should be isotopically enriched to enhance the Mössbauer effect. In the thin absorber approximation ($t_a < 1$), the Mössbauer spectrum can be described by a sum of Lorentzian curves, making easier the theoretical derivations and the fitting procedures of the experimental data. If both source and absorber materials are identical, the Mössbauer spectrum is a single Lorentzian curve centered at zero-velocity relative to the source with a natural linewidth arising from emission and absorption of $2\,\Gamma \approx 0.19$ mm s^{-1} for ^{57}Fe and $2\,\Gamma \approx 0.63$ mm s^{-1} for ^{119}Sn. However, it should be noted that the linewidth is often broadened due to additional effects such as the absorber thickness, self-absorption, imperfections of the spectrometer, etc.

If the source and absorber materials are different, the shape of the Mössbauer spectrum depends on the hyperfine interactions described in Sects. 7.3.2–7.3.4. For the 1/2–3/2 nuclear transition, the observed main changes from the single Lorentzian line obtained for identical source and absorber materials are the following:

– Isomer shift: the single Lorentzian line is shifted by a value that gives the isomer shift relative to the source (or a reference material).
– Quadrupole splitting: the single Lorentzian line is split into a doublet and the line separation gives the quadrupole splitting.
– Magnetic interaction: the single Lorentzian line is split into six lines, the hyperfine magnetic field can be determined from line separation.

The intensity of the spectral lines depends on the nuclear transition probabilities, which gives for example, 3:2:1:1:2:3 intensity ratio for the magnetic sextet of powdered samples. This also depends on the directional dependence of the recoil-free fraction arising from vibrational anisotropy, leading to an asymmetric doublet for the quadrupole effect (Goldanskii-Karyagin effect) [63]. The sample thickness and its texture can also affect the line shape. Finally, it is important to note that combined quadrupole and magnetic interactions or magnetic relaxations may lead to complex spectra.

SnO_2 and SnO have been regarded as negative electrode materials for Li-ion batteries and the electrochemical mechanisms are described in Sect. 7.6.4. The Mössbauer spectra of these two compounds are discussed here to illustrate the effect of hyperfine interactions (Fig. 7.5). Stannic oxide (SnO_2) and stannous oxide (SnO) have $P4_2/mnm$ and $P4/nmm$ tetragonal structures, respectively. They both contain one Sn crystallographic site, which means that the Mössbauer spectra of these two compounds reflect a single Sn environment. In SnO_2, Sn is six-coordinated by O atoms and the Mössbauer spectrum at room temperature is formed by a single peak that can be fitted to a doublet with $\delta = 0$ mm s^{-1} and $\Delta = 0.5$ mm s^{-1}. The value of the isomer shift is typical of Sn(IV) oxidation state while the quadrupole splitting is due to the slightly distorted SnO_6 octahedral environment.

SnO is composed of Sn-O-Sn layers. The Sn local environment can be described by a SnO_4 square based pyramid. The Mössbauer spectrum at room temperature can be fitted to an asymmetric doublet with parameters $\delta = 2.62$ mm s^{-1} and

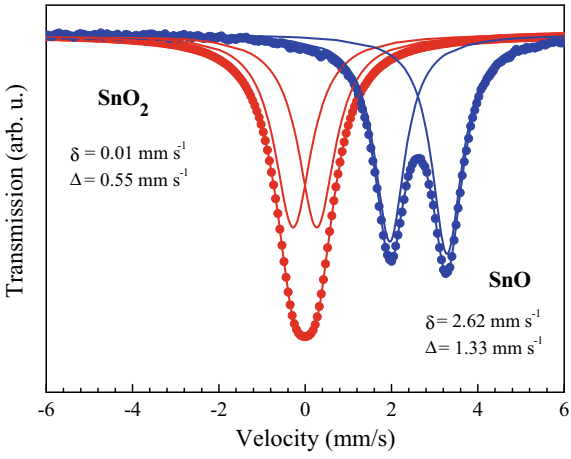

Fig. 7.5 ^{119}Sn Mössbauer spectra of SnO_2 and SnO at room temperature. The experimental data are fitted to two Lorentzian curves, showing a symmetric and unresolved doublet for SnO_2 and an asymmetric doublet for SnO due to the Goldanskii-Karyagin effect

$\Delta = 1.33$ mm s^{-1}. The asymmetry of the doublet is due to the Goldanskii-Karyagin effect arising from the vibrational anisotropy of Sn. The isomer shift of SnO is close to that of βSn (2.56 mm s^{-1}) but must be assigned to Sn(II) oxidation state. Its low value, compared to other Sn(II) species, reflects the hybridization of the Sn valence orbitals that reduces the Sn 5s electron population. The rather high quadrupole splitting is due to the asymmetry of the Sn 5p electrons arising from the SnO_4 local structure that can be related to the existence of a Sn 5p lone pair along the fourfold symmetry axis of the SnO_4 square based pyramid. This axis corresponds to the Z axis of the EFG principal axis system, which leads to $\eta = 0$. According to Eq. (7.10), V_{ZZ} is therefore the only electronic contribution to the quadrupole splitting and Δ reflects the activity of the Sn 5p lone pair.

The area of the resonance absorption line is of primary interest for the application of Mössbauer spectroscopy to batteries. For thin samples containing Mössbauer atoms with the same local environment, the area is proportional to t_a, and therefore, to f_a and n_a. However, the Mössbauer atoms have generally different environments, i.e., different Mössbauer sites as encountered, for example, in crystals with different crystallographic sites, in amorphous phases, or in the different phases of a composite. The different Mössbauer sites, labelled i, give different subspectra that contribute to the overall Mössbauer spectrum. The total area is the sum of the subspectrum areas that are each proportional to $f_i\, n_i$ and a quantitative analysis requires the knowledge or the determination of the different f_i, which cannot be usually achieved.

Many electrode materials are transformed into a multiphase system during the electrochemical reactions and a particular attention must be paid to the evaluation of the recoil-free fractions for a quantitative analysis. For instance, the relative amounts of reactants and products in a Fe^{2+}/Fe^{3+} two-phase reaction can often be obtained by considering the same value of f for the different phases, as in the case of $LiFePO_4/FePO_4$ discussed in Sect. 7.4.2. But this simple assumption fails for some reactions such as the first lithiation of $FeSn_2$ ending with Li_7Sn_2. These two phases contain Sn(0) in different chemical environments, leading to significantly different recoil-free fractions at room temperature $f(FeSn_2)$ and $f(Li_7Sn_2)$. In that case, the relative amounts of $FeSn_2$ and Li_7Sn_2 can only be evaluated at each stage of lithiation from the Mössbauer spectra by considering the ratio $f(FeSn_2)/f(Li_7Sn_2)$ as shown in Sect. 7.6.1.

The existence of a large number of overlapping subspectra can make the distinction between reactants and products difficult, especially for ^{119}Sn Mössbauer spectroscopy. Thus, it is often impossible to determine the Mössbauer parameters for each Mössbauer site in each phase. In that case, more advanced fitting procedures of the Mössbauer data that include hyperfine parameter distributions should be considered, but simplified fitting strategies combined with additional information provided by complementary techniques are often more interesting for the analysis of the electrochemical mechanisms. Such a situation is often encountered with electrode materials in batteries. For instance, Li or Na insertion reactions in positive electrode materials (solid solution) come with the occupation of different vacant sites that can affect selectively the Mössbauer atoms. Another complex situation concerns alloying reactions in tin based negative electrodes

that often produce poorly crystalline and small particles with different compositions. In such cases, simplified fitting procedures are often used in order to highlight some trends in the variations of the Mössbauer parameters as described in Sect. 7.5.3.

7.3.7 In Situ Experiments

The application of ex situ Mössbauer spectroscopy to study electrode materials is similar to the application of this technique in solid-state chemistry as widely described in textbooks [39, 40–42]. However, the products of electrochemical reactions extracted from the electrochemical cells are in powder or film form and can be chemically unstable. Samples must be prepared and handled with care to avoid oxidation or other parasitic reactions. They must be characterized quickly after the electrochemical experiments to reduce a possible evolution due to chemical reactions that could still operate after extraction from the cell even after washing. The low concentration or the low recoil-free fractions of the Mössbauer atoms in the electrode material can be responsible for long-term experiments. In that case, it is possible to use Swagelok-type cells with higher amounts of powdered electrode material, but the measurements are often limited to few cycles. Finally, it should be noted that in many cases, such *post mortem* characterizations of the electrochemical mechanisms provide rather reliable results that can be favorably compared to in situ measurements as shown in Sects. 7.5.3 and 7.6.4.

The in situ Mössbauer experiments are conducted in the same way as the electrochemical measurements except that the commonly used coin cells or Swagelok-type cells are replaced by an electrochemical "in situ cell" for γ-ray transmission. The in situ cells are also based on the "negative electrode-electrolyte-positive electrode" configuration including a separator, but all the components in the path of the γ-rays are optimized to enhance the signal-to-noise ratio and avoid parasitic resonance absorption. This is of particular importance for electrochemical reactions since the time required to record a spectrum, typically several hours, should be consistent with the evolution of the system due to insertion/extraction of typically 0.1 Li or Na per active element and per hour. The commonly encountered difficulties are due to the electrode thickness and the existence of metals or heavy elements in the composition of the cell components.

The in situ Mössbauer measurements are usually performed at room temperature and no special cell designs are required for low or high temperatures. Dunlap et al. used a modified 2325-type coin-cell with thick (1 mm) and thin (250 μm) Be windows for γ-ray transmission (Fig. 7.6) [27, 64]. These windows are electronically conductive and act as current collectors. The thin Be window is coated with the electrode material under study while a lithium foil is placed against the thick window (half-cell configuration). The ^{57}Fe Mössbauer spectra were corrected from the presence of iron in Be windows [27]. A similar cell was proposed by Wattiaux et al. but with Mylar instead of Be windows [65].

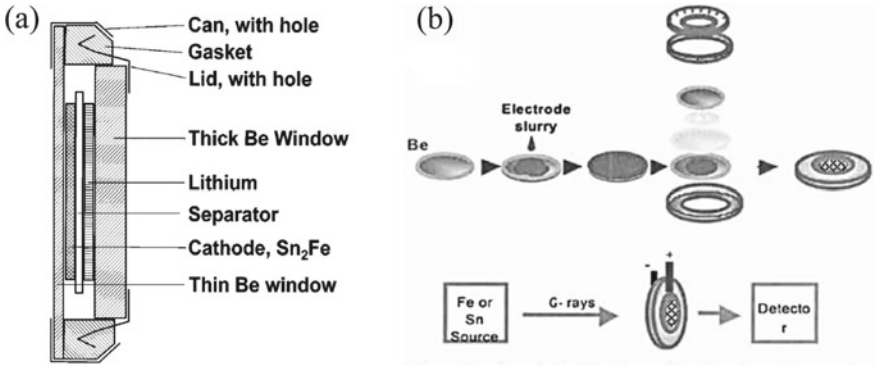

Fig. 7.6 **a** Modified 2325-type coin cell and **b** experimental set up for in situ Mössbauer measurements. **a** Reprinted with permission from Ref. [27]. Copyright 1999 American Physical Society. **b** Image courtesy Mössbauer Effect Data Centre, Dalian Institute of Chemical Physics, Chinese Academy of Sciences [64]

Ariyoshi et al. proposed an aluminum-laminated polyethylene bag containing Li metal with stainless steel sheet as current collector placed outside the γ-ray beam and working electrode on aluminum foil [66]. A pouch cell was also used by Ionica et al. consisting of an airtight aluminized plastic bag with electrodes made according to the Bellcore technology [67].

Chamas et al. used a modified Swagelok tube union with PMMA windows transparent to γ-rays, called Cell 1 in this chapter, and less fragile than Be windows to maintain the cohesion of the internal cell configuration [68]. The electrodes are lithium foil and powdered active material spread on a Be window for electronic conduction. They are both in electrical contact with hollow steel tubes as cell terminals (Fig. 7.7a). Such a cell is interesting for the characterization of powdered alloying or conversion materials that suffer from large volume variations. Another type of Swagelok cell, called Cell 2 in this chapter, as first proposed for in situ XRD measurements in reflection mode [69], was modified for γ-ray transmission (Fig. 7.7b). A similar cell but with a large Be window in contact with the active material was used in both reflection and transmission geometries, making combined XRD and Mössbauer measurements possible [70].

A potentiostat-galvanostat system is used to apply and control the voltage or current to the in situ electrochemical half-cell. Most of the operando Mössbauer experiments are carried out in galvanostatic regime, i.e. by imposing a constant current, in order to insert a constant number of Li^+ or Na^+ ions per time unit in the working electrode. The acquisition time of an operando Mössbauer spectrum should be rather short to have a snapshot of the electrochemical reaction but should also be rather long for a good signal-to-noise ratio. The acquisition time depends on the current injected to the cell that should be as low as possible to approach thermodynamic equilibrium conditions. However, a too low current leads to long-term experiments, typically more than several weeks per electrochemical cycle, which

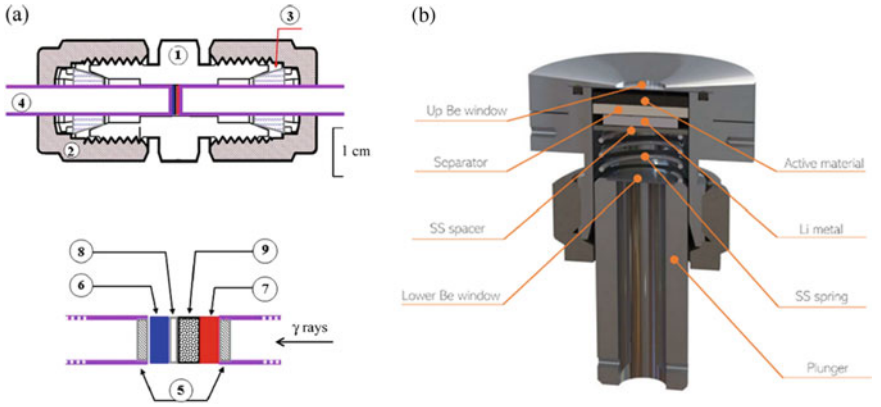

Fig. 7.7 **a** Cell 1. Modified Swagelok cell composed of PFA cell body (1), nuts (2), PFA sealing ferrules (3) and stainless steel plungers (4). The junction around the electrodes is formed by PMMA windows (5), lithium disc (6), Be based connector (7), Whatman separator (8) and active material (9). Reprinted with permission from Ref. [68]. Copyright 2013 American Chemical Society. **b** Cell 2. Modified Swagelok cell for in situ Mössbauer spectroscopy used in transmission mode designed by S4R France

can be a severe issue for the airtightness of the cell. Although it could be interesting to use high currents for the analysis of kinetic effects, such experiments are made difficult by the too long period of time required to record reliable spectra compared to the fast evolution of the insertion and extraction processes. In most cases, the mass of electrode materials is around 1–10 mg. Typical currents in the range of 10^{-2}–10^{-1} Li^+ (or Na^+) per active element and per hour and measurement times in the range of 1–10 h per spectrum generally provide a good compromise between the total duration of operando experiments and a correct signal-to-noise ratio. But this obviously depends on the experimental set-up and the concentration of Mössbauer atoms in the electrode material.

To increase the acquisition time of each operando spectrum and/or perform measurements in thermodynamic equilibrium conditions, while maintaining a reasonable time for the overall electrochemical experiment, specific current profiles should be considered. For instance, the current can be stopped at regular periods of time for voltage relaxation during which the Mössbauer spectra are recorded. Compared to the galvanostatic protocol, the acquisition time of each spectrum is longer and a better signal-to-noise ratio is obtained. However, the number of spectra recorded during the charge-discharge cycles is usually smaller, which can be a limitation for monitoring electrochemical reactions. These two approaches are compared in Sect. 7.4.1.

7.4 Insertion Reactions

7.4.1 Solid-Solution Reactions

The solid-solution reactions refer to the insertion of Li^+ or Na^+ ions on the vacant sites of a solid without phase transition. To illustrate the application of Mössbauer spectroscopy, the example considered here is the Nasicon-type (sodium super ionic conductor) compound $Na_{1.5}Fe_{0.5}Ti_{1.5}(PO_4)_3$ proposed as electrode material for Na-ion batteries and studied with two different operando protocols [71, 72]. $Na_{1.5}Fe_{0.5}Ti_{1.5}(PO_4)_3$ sub-micrometer particles were obtained by solid-state reaction and coated with carbon to improve the electronic conductivity. The crystallinity was controlled by XRD while DFT calculations confirmed the preferential occupation of some vacant sites by Na in the pristine material. The crystal has a rhombohedral $R\bar{3}c$ structure with a random occupation of the metal sites (12c) by 25% Fe and 75% Ti. The ^{57}Fe Mössbauer spectrum of $Na_{1.5}Fe_{0.5}Ti_{1.5}(PO_4)_3$ consists of a doublet due to high spin Fe^{3+} while the spectrum of the C-coated sample $Na_{1.5}Fe_{0.5}Ti_{1.5}(PO_4)_3$/C was fitted to two doublets with Mössbauer parameters: $\delta = 0.42$ mm s^{-1}, $\Delta = 0.28$ mm s^{-1} assigned to high spin Fe^{3+} (91%) and $\delta = 1.18$ mm s^{-1}, $\Delta = 2.37$ mm s^{-1} assigned to high spin Fe^{2+} in impurities arising from pyrolysis (9%).

The voltage curve of the first cycle of $Na_{1.5}Fe_{0.5}Ti_{1.5}(PO_4)_3$/C based electrode, with carbon black as electronic additive and PVDF binder, in a Na half-cell with galvanostatic current of 0.1 Na per fu (formula unit) and per hour shows a voltage hysteresis at about 2.2 V with a weak polarization (Fig. 7.8).

During the sodiation, the voltage decreases from 2.5 to 2.2 V for the first 0.5 Na (Region R1) and then forms a plateau until the end of sodiation at 2 Na (Region R2). The desodiation curve is similar except for a small irreversibility of 0.1 Na. The shape of the sodiation curve suggests a two-step mechanism consisting in the formation

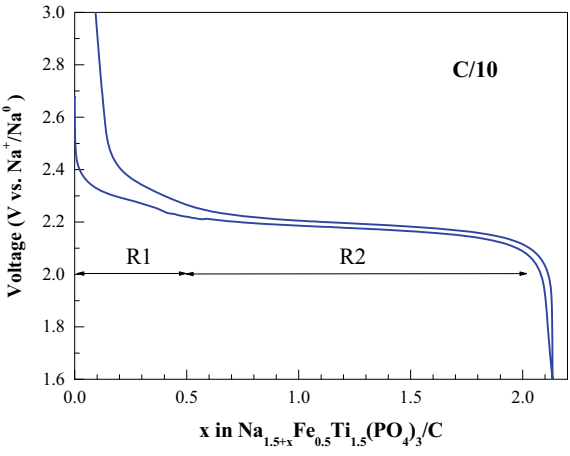

Fig. 7.8 Voltage curve of the first cycle of $Na_{1.5}Fe_{0.5}Ti_{1.5}(PO_4)_3$/C in a Na half-cell at C/10 rate (0.1 Na per fu and per hour) showing two different mechanisms in regions R1 and R2. Reprinted with permission from Ref. [71]. Copyright 2015 American Chemical Society

of a solid solution (R1) followed by a two-phase reaction (R2). This mechanism is reversible for desodiation. The voltage curve differs from that of $NaTi_2(PO_4)_3$ formed by a plateau at 2.2 V, which was assigned to a two-phase reaction corresponding to the redox couple Ti^{4+}/Ti^{3+} [73]. The operando XRD patterns in region R1 are almost identical to the XRD pattern of the pristine material with $R\bar{3}c$ structure while the sodiation in R2 shows two phases with $R\bar{3}c$ and $P\bar{1}c$ structures. These results are consistent with the mechanism suggested by the voltage profile but do not reveal the redox mechanism.

Operando ^{57}Fe Mössbauer measurements were carried out with the Cell 2 described in Sect. 7.3.7 and two different protocols. In the first protocol, the spectra were recorded continuously during the first cycle in galvanostatic regime with a current of 0.04 Na per fu and per hour and an acquisition time of 2 h per spectrum. In the second protocol, a periodic current was imposed. Each 16-h period consisted of a constant current of 0.1 Na per fu and per hour during 4 h and a zero current (open circuit condition) during 12 h for recording the spectrum in order to improve the signal-to-noise ratio. The spectra show that in R1 the Fe^{3+} doublet of $Na_{1.5}Fe_{0.5}Ti_{1.5}(PO_4)_3$ ($\delta = 0.41$ mm s^{-1}, $\Delta = 0.34$ mm s^{-1}) is transformed into a Fe^{2+} doublet ($\delta \approx 1.2$ mm s^{-1}, $\Delta \approx 2.0$ mm s^{-1}) (Fig. 7.9).

The total area of the spectra does not vary noticeably during the sodiation-desodiation process, indicating that the recoil-free fractions of Fe^{2+} and Fe^{3+} have close values. Thus, the relative contributions of the Fe^{2+} and Fe^{3+} subspectra to the Mössbauer spectra can be regarded as the relative amounts of Fe^{2+} and Fe^{3+} ions in the electrode material. The amount of Fe^{3+} linearly decreases in R1 while the amount of Fe^{2+} increases (Fig. 7.10). In R2, the variations are not significant and the amounts of Fe^{3+} and Fe^{2+} are almost constant, showing that sodiation does not change the oxidation state of iron anymore. The variations are reversible for desodiation with strong changes at the end of the process. It should be noted that the values of the relative contributions of Fe^{2+} and Fe^{3+} are more dispersed for the galvanostatic protocol, which confirms the better quality of the data obtained with the other protocol. These results show that the mechanism of sodiation consists in the formation of a solid solution coming with the reduction of Fe^{3+} into Fe^{2+}, followed by a two-phase reaction leading to the reduction of Ti^{4+} into Ti^{3+}. The mechanism is reversible for desodiation. The cyclability and rate capability are better for $Na_{1.5}Fe_{0.5}Ti_{1.5}(PO_4)_3$ compared to $NaTi_2(PO_4)_3$, which can be attributed to enhanced Na diffusion due to the single-phase reaction in R1.

The operando Mössbauer spectroscopy provides a quantitative characterization of the redox reactions but cannot distinguish between solid-solution and two-phase reactions. This is obtained by operando XRD. Thus, the combined use of these two techniques successfully explains the two-step mechanism by the reactions

$$Na_{1.5}Fe_{0.5}^{3+}Ti_{1.5}^{4+}(PO_4)_3\left[R\bar{3}c\right] + 0.5Na = Na_2Fe_{0.5}^{2+}Ti_{1.5}^{4+}(PO_4)_3\left[R\bar{3}c\right] \quad (7.19)$$

$$Na_2Fe_{0.5}^{2+}Ti_{1.5}^{4+}(PO_4)_3\left[R\bar{3}c\right] + 1.5Na = Na_{3.5}Fe_{0.5}^{2+}Ti_{1.5}^{3+}(PO_4)_3\left[P\bar{1}c\right] \quad (7.20)$$

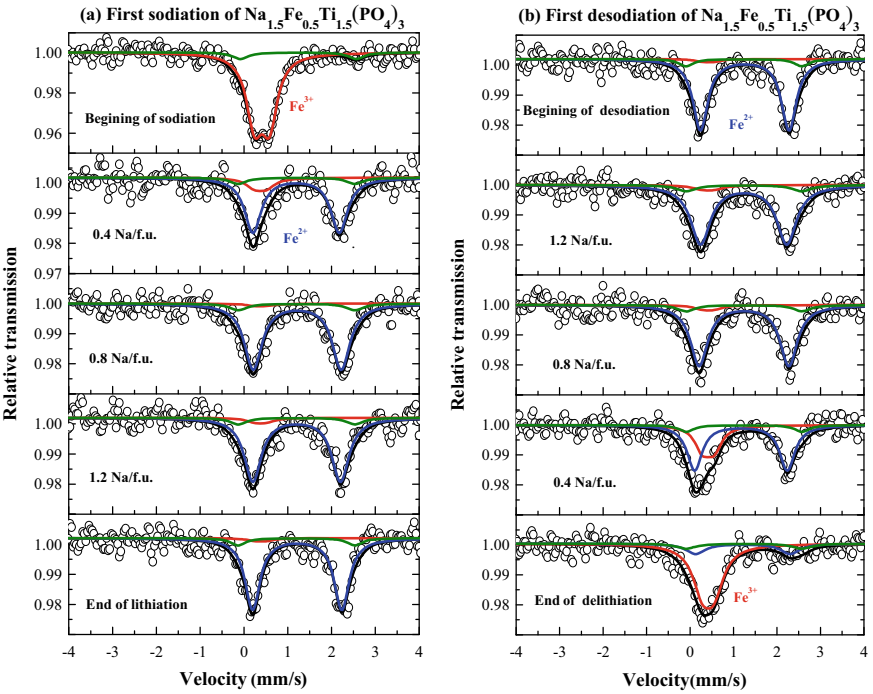

Fig. 7.9 Operando ^{57}Fe Mössbauer spectra obtained for the first sodiation and desodiation of $Na_{1.5}Fe_{0.5}Ti_{1.5}(PO_4)_3$/C in Cell 2. Galvanostatic regime (0.1 Na per fu and per hour), stopped every 0.4 Na for measurement during 12 h (open circuit). Reprinted with permission from Ref. [71]. Copyright 2015 American Chemical Society

Other applications of Mössbauer spectroscopy to solid-solution reactions in batteries can be found in Ref. [74–79].

7.4.2 Two-Phase Reactions

Lithium transition metal phosphates with olivine structure have been regarded as positive electrode materials of Li-ion batteries for a long time and $LiFePO_4$ based batteries are now widely commercialized. Although this material has lower specific capacity and operating voltage than commonly used layered metal oxides, it shows better specific power, safety and cycle life. In addition, $LiFePO_4$ is less expensive than Co-based materials and environmentally friendly.

The electrochemical mechanism can be easily studied by ^{57}Fe Mössbauer spectroscopy. The voltage profile of a $LiFePO_4$ based electrode in a Li half-cell obtained in galvanostatic regime shows two similar plateaus at about 3.4 V for delithiation and lithiation, suggesting the existence of a reversible two-phase reaction.

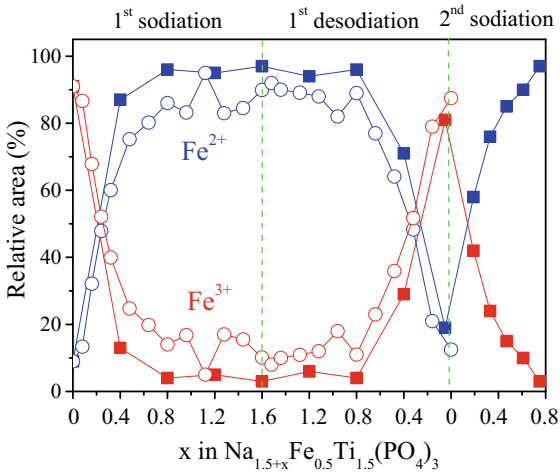

Fig. 7.10 Variations of the relative contributions of Fe^{2+} and Fe^{3+} to the ^{57}Fe Mössbauer spectra obtained for the 1st sodiation (x = 0–1.6), the 1st desodiation (x = 1.6–0) and the beginning of the 2nd sodiation (x = 0–0.8) of $Na_{1.5+x}Fe_{0.5}Ti_{1.5}(PO_4)_3$ in Cell 2. Galvanostatic regime (open circles) and mixed galvanostatic-open circuit regime (solid squares). Regions R1 and R2 shown in Fig. 7.8 correspond to x < 0.5 and x > 0.5, respectively. Reprinted with permission from Ref. [71]. Copyright 2015 American Chemical Society

The operando ^{57}Fe Mössbauer spectra recorded at room temperature at the beginning and at the end of the first delithiation are formed by a doublet with Mössbauer parameters: $\delta = 1.22$ mm s^{-1}, $\Delta = 2.96$ mm s^{-1} and $\delta = 0.42$ mm s^{-1}, $\Delta = 1.52$ mm s^{-1}, respectively, that are typical of high spin Fe^{2+} and Fe^{3+} in $LiFePO_4$ and $FePO_4$, respectively (Fig. 7.11). $LiFePO_4$ and $FePO_4$ are antiferromagnetic below 52 K and 125 K [80], respectively, and the observed doublets are consistent with the paramagnetic state for both compounds at room temperature.

The origin of the Mössbauer parameters was analyzed by DFT-LAPW calculations [46]. The calculated electron density at the nucleus increases from $LiFePO_4$ to $FePO_4$, which is consistent with the decrease of the number of Fe 3d electrons from Fe^{2+} to Fe^{3+}, as expected from the shielding effect described in Sect. 7.3.2. The observed decrease of the isomer shift from $LiFePO_4$ to $FePO_4$ is due to the negative sign of $\Delta\langle r_n^2\rangle$ for ^{57}Fe.

The EFG strongly depends on charge anisotropy, and therefore, on the occupation of the Fe $3d_\uparrow$ and Fe $3d_\downarrow$ states by the valence electrons. For instance, the calculated main EFG component of Fe in $LiFePO_4$ is lower for low spin Fe^{2+} (formally $3d_\uparrow{}^3 3d_\downarrow{}^3$): $|V_{ZZ}| \approx 3\ 10^{21}$ V m^{-2} than for high spin Fe^{2+} (formally $3d_\uparrow{}^5 3d_\downarrow{}^1$): $V_{ZZ} \approx 14\ 10^{21}$ V m^{-2}. As shown by Eq. (7.10), the value of the quadrupole splitting mainly depends on V_{ZZ}. For $LiFePO_4$, all the Fe $3d_\uparrow$ states are occupied and the anisotropy is due to the Fe $3d_\downarrow$ charge distribution. For $FePO_4$, only the Fe $3d_\uparrow$ states are occupied, leading to a small Fe 3d electron anisotropy and the quadrupole splitting mainly arises from the asymmetry of the FeO_6 octahedra distorted by the

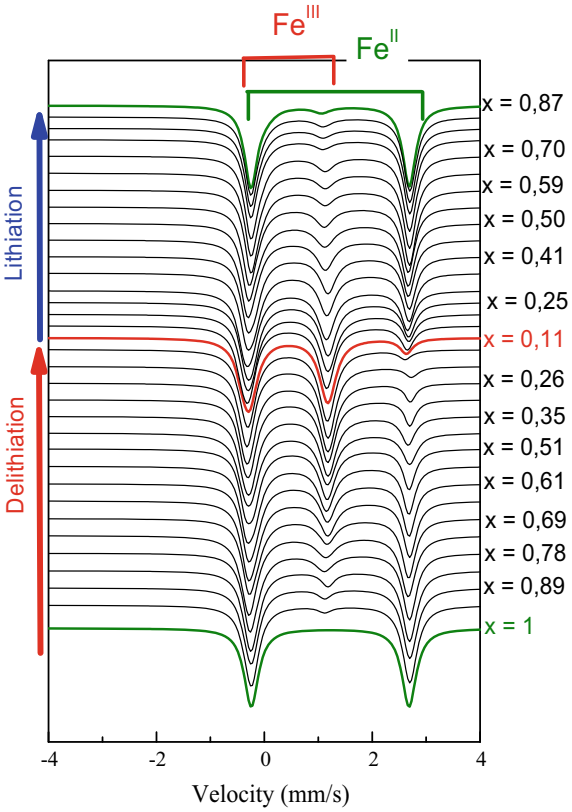

Fig. 7.11 Operando ^{57}Fe Mössbauer spectra (fitted curves) obtained for the first delithiation-lithiation cycle of Li_xFePO_4 in Cell 2

P-O bonds. This structural distortion in $FePO_4$ has a smaller effect on the value of V_{ZZ} than the Fe $3d_{\downarrow}$ valence electron anisotropy in $LiFePO_4$, which explains that the quadrupole splitting of $FePO_4$ is lower than that of $LiFePO_4$, as often encountered for high spin Fe^{3+} and Fe^{2+} in iron phosphates and oxides.

All the Mössbauer spectra recorded during the delithiation and lithiation of $LiFePO_4$ were succesfully fitted to a linear combination of the doublets of $LiFePO_4$ and $FePO_4$ [81]. Since the recoil-free fractions are similar for these two compounds [82], the relative amounts of $LiFePO_4$ and $FePO_4$ are given by the relative contributions of the two subspectra. The observed variations are linear (Fig. 7.12), in line with the reversible two-phase reaction

$$FePO_4 + Li^+ + e^- = LiFePO_4 \tag{7.21}$$

This shows that Mössbauer spectroscopy can be used as a quantitative tool to evaluate the relative amounts of reactants and products of a two-phase electrochemical reaction.

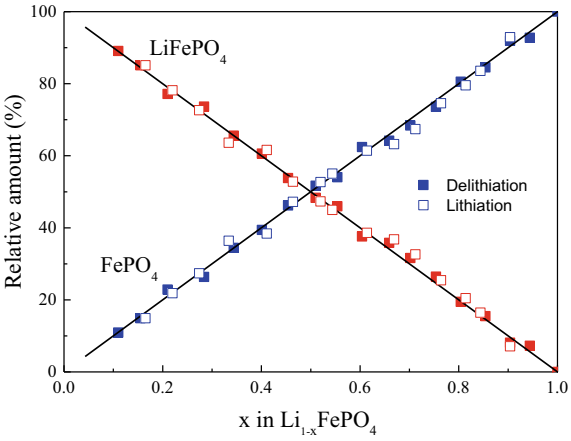

Fig. 7.12 Variations of the relative amounts of $LiFePO_4$ and $FePO_4$ obtained from operando ^{57}Fe Mössbauer spectra for the first delithiation and lithiation of $LiFePO_4$

The substitution of Mn or Co for Fe was proposed to increase the electrode potential and, consequently, the energy density of the battery. The mechanism is more complex than that of $LiFePO_4$ since it involves not only the Fe^{3+}/Fe^{2+} redox couple but also Mn^{3+}/Mn^{2+} or Co^{3+}/Co^{2+}. For example, the voltage curves of $LiFe_{0.75}Mn_{0.25}PO_4$ and $LiFe_{0.25}Mn_{0.75}PO_4$ are both formed by two successive plateaus at about 3.4 and 4 V. The analysis of the ^{57}Fe Mössbauer spectra shows that these two plateaus can be attributed to two-phase reactions corresponding to the redox couples Fe^{3+}/Fe^{2+} and Mn^{3+}/Mn^{2+}, respectively. The observed transition region between the two plateaus was attributed to a solid-solution reaction [83, 84]. Other studies of two-phase reactions in batteries by Mössbauer spectroscopy can be found in Ref. [85–88].

7.5 Alloying Reactions

7.5.1 Negative Electrode Materials for Li-Ion Batteries

Negative electrode materials containing elements that form alloys with lithium have been proposed to increase the electrode capacity and avoid the formation of lithium dendrites. Many chemical elements of the groups 13–15 of the periodic table can reversibly react with lithium at room temperature in liquid organic electrolyte based cells [89]. The two most interesting and studied elements are Si and Sn that can be used as high capacity and low voltage electrode materials. They are rather abundant and environmentally benign. The lithiation-delithiation reactions of Si and βSn lead to the reversible formation of Li_xSi and Li_ySn alloys or compounds, respectively, with the usually accepted maximum values $x = 3.75$ and $y = 4.4$. By considering these values, the volumetric capacities evaluated at the state of full lithiation are of about 2200 mA h cm^{-3} (Si) and 2100 mA h cm^{-3} (βSn) and the specific capacities

are 3580 mA h g^{-1} (Si) and 990 mA h g^{-1} (βSn) [89]. These values are significantly higher than the theoretical values of ~800 mA h cm^{-3} and 372 mA h g^{-1} for graphite that accommodates only 1 Li per 6 C.

However, there is a crucial issue with alloying reactions. In contrast to Li intercalation between graphite layers that leads to about 10% volume changes, alloying reactions suffer from strong volume variations of about 300% for Si/$Li_{3.75}$Si and Sn/$Li_{4.4}$Sn transformations. This causes mechanical (electrode film cracks), electrical (loss of electrical contacts) and chemical (SEI instabilities) degradations, reducing significantly the cycling performance of electrodes. Different approaches have been proposed to overcome this problem by improving the electrode formulation (binder, conductive additives), the electrolyte, or the electrochemically active materials. In the latter case, this includes particle size reduction (nanoparticles), particle coating, dispersion of the active particles within the pristine material (composite), and in situ dispersion of the active species during the first electrochemical cycles. The electrochemical reactions taking place in these systems are rather complex and some examples of the application of Mössbauer spectroscopy to elucidate such mechanisms are given in Sect. 7.6.

The present section deals with Li-Sn and Na-Sn alloying reactions. Although Si is not a Mössbauer element, previous investigations of Si_xSn amorphous phases successfully provided information on Li-Si alloying reactions as shown in Sect. 7.5.4.

7.5.2 βSn as Negative Electrode Material for Li-Ion Batteries

The experimental voltage curves of βSn in a Li half-cell obtained in galvanostatic regime at low current density show different plateaus that can be attributed to two-phase reactions (Fig. 7.13) [90]. These plateaus are observed for both lithiation and delithiation processes, showing the reversibility of the mechanism.

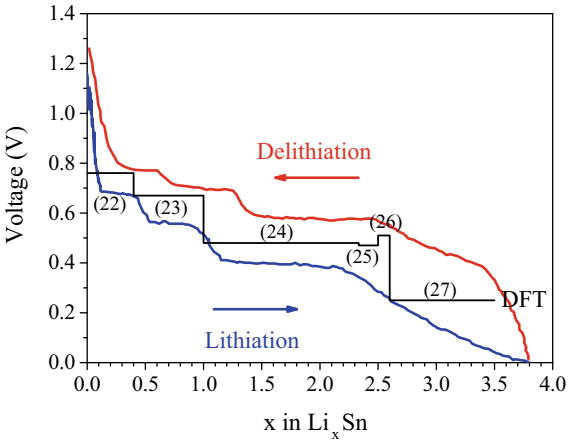

Fig. 7.13 Experimental voltage curves for the first cycle of βSn in a Li half-cell [90] and DFT-GGA voltage profile for the reactions (7.22)–(7.27)

The theoretical voltage profile of βSn was determined by DFT calculations [24, 90] by considering the different crystalline phases of the Li-Sn phase diagram [91] and the following reactions

$$5\ \beta\text{Sn} + 2\ \text{Li} \rightarrow \text{Li}_2\text{Sn}_5 \tag{7.22}$$

$$\text{Li}_2\text{Sn}_5 + 3\ \text{Li} \rightarrow 5\ \text{LiSn} \tag{7.23}$$

$$3\ \text{LiSn} + 4\ \text{Li} \rightarrow \text{Li}_7\text{Sn}_3 \tag{7.24}$$

$$2\ \text{Li}_7\text{Sn}_3 + \text{Li} \rightarrow 3\ \text{Li}_5\text{Sn}_2 \tag{7.25}$$

$$5\ \text{Li}_5\text{Sn}_2 + \text{Li} \rightarrow 2\ \text{Li}_{13}\text{Sn}_5 \tag{7.26}$$

$$2\ \text{Li}_{13}\text{Sn}_5 + 9\ \text{Li} \rightarrow 5\ \text{Li}_7\text{Sn}_2 \tag{7.27}$$

The comparison between the experimental and theoretical voltage profiles suggests that the two first plateaus at average experimental voltages of 0.75 V and 0.65 V can be explained by Eqs. (7.22) and (7.23) corresponding to the successive formations of Li_2Sn_5 and LiSn, respectively. These results were confirmed by in situ XRD. The following plateau at about 0.5 V can be attributed to Eqs. (7.24)–(7.26) and the possible formation of Li_7Sn_3, Li_5Sn_2 and/or $Li_{13}Sn_5$. These three phases cannot be distinguished in the experimental voltage profile because they have closed compositions and formation energies. The theoretical voltage plateau arising from the formation of Li_7Sn_2, as given by Eq. (7.27), is not observed experimentally since the voltage curve shows a continuous decrease in the range 2.2–3.8 Li per Sn. Based on the simulation of the XRD patterns, this decrease was interpreted by the formation of a metastable phase with a BCC disordered structure that shows the same short-range order as $Li_{22}Sn_5$ [90]. These results show that the Sn-rich Li_xSn crystalline equilibrium phases are reversibly formed during the lithiation of βSn while the Li-rich Li_xSn phases could be metastable. It should be noted that the electrochemical mechanisms in Li-ion batteries are also affected by other processes such as low atomic diffusion within the electrode material, side reactions with the electrolyte, kinetic effects, etc. In addition, the Li_xSn phases resulting from the lithiation of Sn based electrodes are poorly crystallized and of small size, which makes the analysis by XRD difficult. Thus, the ^{119}Sn Mössbauer spectroscopy, which is sensitive to the Sn local environment, is a great alternative tool for the characterization of the Li_xSn phases.

7.5.3 Li_xSn Reference Materials

To identify the lithiated products resulting from the Li-Sn alloying reactions by ^{119}Sn Mössbauer spectroscopy, it is convenient to determine the Mössbauer parameters of the equilibrium crystalline phases considered as references. Different experimental Li-Sn phase diagrams were reported and the currently accepted one shows the existence of seven crystalline phases: Li_2Sn_5, LiSn, Li_7Sn_3, Li_5Sn_2, $Li_{13}Sn_5$, Li_7Sn_2 and $Li_{22}Sn_5$, [91], although the latter phase should be better described by $Li_{17}Sn_4$ [92]. Li_8Sn_3 was also observed and should be included in the Li-Sn phase diagram but is not considered here [93]. Finally, other compositions or structures were predicted by DFT calculations but have not been experimentally observed yet [94–96]. In line with previously reported works [97, 98], only the seven crystalline phases given above are considered here as references. The crystal structures of all the phases were experimentally determined by XRD and show the existence of one (Li_5Sn_2), two (Li_2Sn_5, LiSn, Li_7Sn_2), three (Li_7Sn_3, $Li_{13}Sn_5$) and four ($Li_{22}Sn_5$) Sn crystallographic sites. The Mössbauer spectra were reported by two groups using different synthesis methods: high temperature solid-state reactions [97] and mechanosynthesis followed by annealing [98]. The contributions of the different Sn crystallographic sites cannot be easily distinguished in the spectra that are unresolved and contain the contributions of tin based impurities (Fig. 7.14).

The comparison between the values of the Mössbauer parameters obtained by the two groups shows some small variations that can be attributed to differences in the purity and crystallinity of the materials (Table 7.1).

The relative contributions of the subspectra, when not fixed, are consistent with the crystallographic site multiplicities. The values of the quadrupole splitting reflect the different Sn local environments due to the existence of different nearest neighbors (Li, Sn), polyhedral geometries and bond lengths. Finally, the values of the isomer shift averaged over the different Sn crystallographic sites, δ_{av}, are of about 2.4 mm s^{-1} for the two Sn-rich Li_xSn phases and decrease from 2.1 to 1.8 mm s^{-1} with increasing relative amount of Li for the Li-rich Li_xSn phases (Fig. 7.15). These values are all in the range of the Sn(0) oxidation state and can be correlated to the number of Sn-Sn bonds. The two ranges of isomer shifts reflect the existence of Sn based sub-lattices for the Sn-rich Li_xSn phases and Sn single atoms or clusters of two or three Sn atoms bonded to Li atoms for the Li-rich Li_xSn phases.

It is also interesting to plot the values of the average isomer shift of the Li_xSn references as a function of the number of Li per Sn (Fig. 7.15). The observed linear correlation suggests that $\delta_{av}(x)$ strongly depends on the average composition of Li_xSn but not on crystal structure. This means that such a correlation can be used to evaluate x from the measurement of δ_{av} for Li_xSn amorphous phases or small particles as often encountered during the lithiation-delithiation processes of Sn based electrodes.

The linear variations of $\delta_{av}(x)$ can be related to changes in the numbers of Sn 5s (N_{5s}) and Sn 5p (N_{5p}) electrons. The values of $\rho(0)$, N_{5s} and N_{5p} were evaluated with the DFT-LAPW method. Following the procedure described in Sect. 7.3.2, the theoretical values of δ were obtained from $\rho(0)$ and the calibration constant

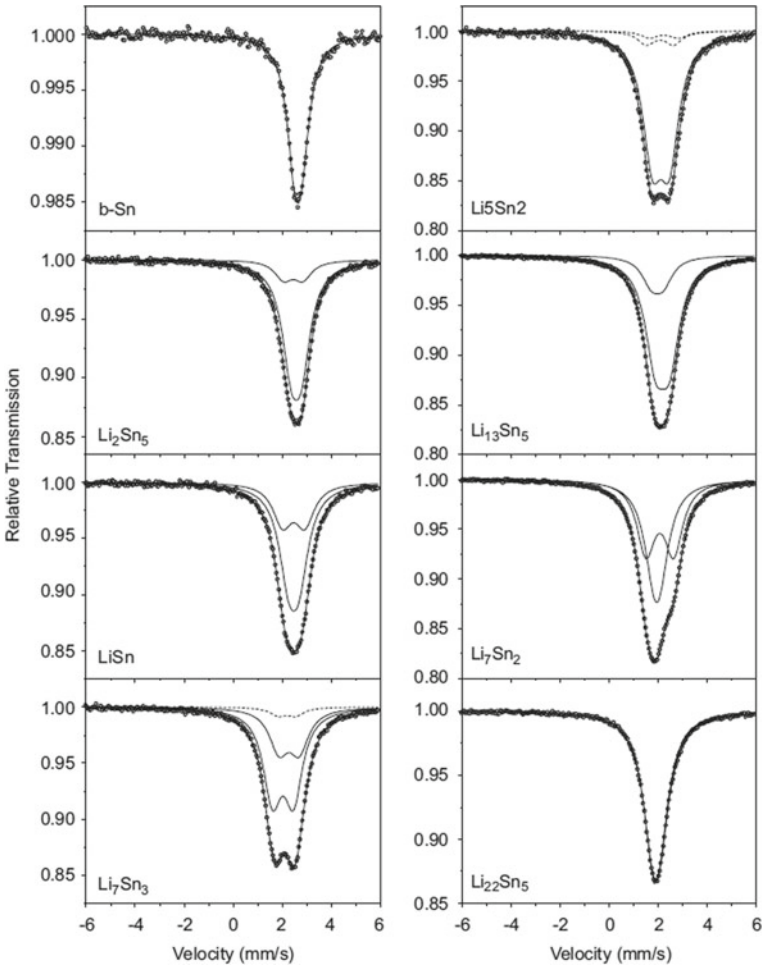

Fig. 7.14 ^{119}Sn Mössbauer spectra of Li_xSn crystalline references measured at room temperature. Reprinted from Ref. [98]. Copyright 2007, with permission from Elsevier

α (Eq. 7.4). The experimental and theoretical averaged values of the isomer shift, δ_{av}, are in good agreement and the theoretical values of $\delta_{av}(x)$ linearly increase with N_{5s} (Fig. 7.16a) and decrease with N_{5p} (Fig. 7.16b) in line with Eq. (7.5).

The variations of N_{5p} (~0.25) are larger than those of N_{5s} (~0.1) and they both linearly contribute to the variations of δ_{av}. The increase of N_{5p} with x reflects the increase of the electron transfer from Li to Sn due to the increase number of Li atoms around each Sn.

Empirical correlation rules were previously proposed for Mössbauer parameters, such as the Δ-δ correlation diagram used to predict the electrochemical activity of tin based electrode materials for Li-ion batteries [99]. In the present case, an empirical

Table 7.1 Values of the ^{119}Sn Mössbauer parameters of Li_xSn crystalline references obtained at room temperature by Dunlap et al. [97] and by Robert et al. [98]. The values of the isomer shift, δ, relative to $BaSnO_3$ and the quadrupole splitting, Δ, are given for the different Sn crystallographic sites

	βSn	Li_2Sn_5	LiSn	Li_7Sn_3	Li_5Sn_2	$Li_{13}Sn_5$	Li_7Sn_2	$Li_{22}Sn_5$
δ/Δ(mm/s) (crystallographic sites) [97]	2.56/0 (4a)	2.53/0.49 (8i) 2.23/0.67 (2d)	2.42/0.41 (2 m) 2.41/1.09 (1a)	2.17/0.46 (2e) 2.09/1.19 (2e,2e)	2.02/0.67 (6c)	1.93/0.33 (1a) 2.04/0.39 (2d) 2.05/0.97 (2d)	1.90/0.40 (4i) 1.95/1.33 (4 h)	1.84/0.27 (16e, 16e, 24f, 24g)
δ/Δ(mm/s) (crystallographic sites) [98]	2.56/0.29 (4a)	2.49/042 (8i) 2.36/0.78 (2d)	2.38/0.43 (2 m) 2.38/0.91 (1a)	2.19/0.82 (2e) 1.94/0.86 (2e,2e)	2.01/0.69 (6c)	1.86/0.48 (1a) 2.07/0.58 (2d,2d)	1.84/0.28 (4i) 1.96/1.13 (4 h)	1.83/0.31 (16e, 16e, 24f, 24g)

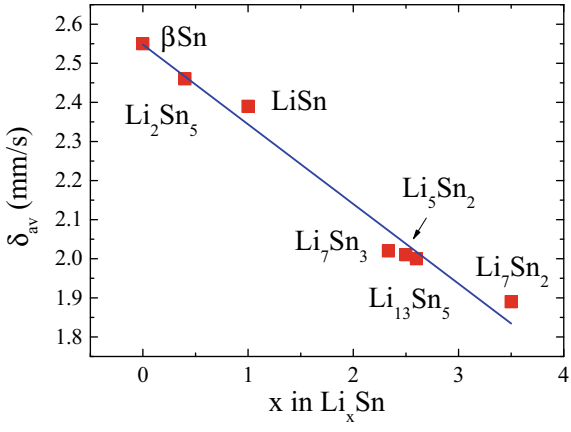

Fig. 7.15 Average experimental values of the isomer shift of Li_xSn crystalline references, δ_{av}, as a function of the number of Li per Sn, x, and regression line (blue)

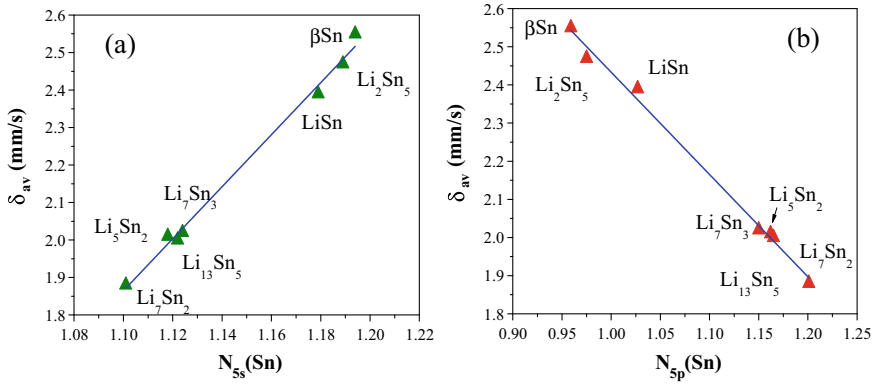

Fig. 7.16 Correlations between the experimental values of the isomer shift and the DFT numbers of Sn 5s electrons **a** and Sn 5p electrons **b** for Li_xSn crystalline references, and linear regression lines (blue)

relation between the average isomer shift of Li_xSn and x can be derived from the values obtained for the reference crystalline phases by considering the regression line shown in Fig. 7.15:

$$\delta_{av}(x) = 2.55 - 0.20x \tag{7.28}$$

From this equation, it is possible to determine x from δ_{av}, which gives the average composition of the Li_xSn species in the electrode materials when they cannot be identified as shown for the delithiation of $FeSn_2$ based electrodes in Sect. 7.6.1.

The ^{119}Sn Mössbauer spectroscopy was used for ex situ measurements at different stages of the first lithiation of βSn electrode in a Li half-cell [100]. The voltage profile is similar to that of Fig. 7.13, except at the very beginning of lithiation due to the

existence of tin oxides as impurities. The spectra recorded for the insertion of 0.5, 1 and 3.4 Li per Sn were fitted to two doublets with Mössbauer parameters similar to those of Li_2Sn_5, LiSn and Li_7Sn_2, respectively, although some small differences could be tentatively attributed to variations in the composition of the electrochemically formed Li_xSn phases.

7.5.4 Si as Negative Electrode Material for Li-Ion Batteries

The electrochemical alloying reactions of Li with Si were studied by in situ ^{119}Sn Mössbauer spectroscopy for amorphous a-Si_ySn_{1-y} (y = 0.87, 0.93) powdered samples obtained by magnetron sputtering [101]. The voltage profiles of the two a-Si_ySn_{1-y} phases differ from that of βSn but are similar to that of amorphous Si (a-Si), showing two sloping plateaus with a transition at ~2.3 Li (Fig. 7.17a). The same electrochemical behaviors observed for a-Si and a-Si_ySn_{1-y} suggest that similar reactions take place in the two electrode materials, justifying the use of Sn as Mössbauer probe in a-Si [102, 103].

The operando Mössbauer spectra of $Li_xSi_{0.87}Sn_{0.13}$ obtained during the first lithiation-delithiation cycle consist of a single line or a doublet around 2 mm s^{-1}

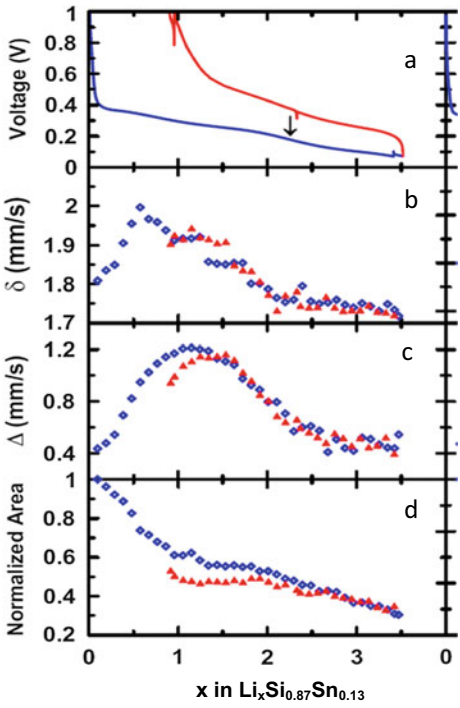

Fig. 7.17 **a** Voltage curves of a-$Si_{0.87}Sn_{0.13}$ in a Li half-cell. **b** Variations of the isomer shift δ, **c** quadrupole splitting Δ and **d** total area of the ^{119}Sn Mössbauer spectra recorded during the first lithiation (blue) and delithiation (red). Image courtesy Mössbauer Effect Data Centre, Dalian Institute of Chemical Physics, Chinese Academy of Sciences [64]

[101]. All the spectra were successfully fitted to a doublet and the Mössbauer parameters strongly change during lithiation (Fig. 7.17). Similar variations are obtained for delithiation, showing the reversibility of the mechanism.

From $x = 0$ to $x = 1$, the isomer shift increases from 1.8 to 2 mm s^{-1} and the quadrupole splitting increases from 0.4 to 1.2 mm s^{-1}. The value $\delta = 1.8$ mm s^{-1} is close to that of αSn and characteristic of Sn(0) in tetrahedral environment, as expected for sp^3 hybridization in a-Si. This confirms the substitution of Sn for Si in a-Si and the absence of βSn. The values of isomer shift obtained for $x < 1$ are lower than 2 mm s^{-1}, which excludes the formation of Sn-rich Li_xSn alloys. The increase of δ from 1.8 to 2 mm s^{-1} is mainly due to the increase of N_{5s} (see Eq. 7.5) arising from the electronic transfer from Li to Sn, which indicates the substitution of Li for Si as first nearest neighbors of Sn. The progressive increase in the number of Li atoms around Sn makes the Sn tetrahedral environments formed by Li and Si atoms more asymmetrical, in agreement with the observed increase of the quadrupole splitting.

From $x = 1$ to $x = 2.3$, the isomer shift and quadrupole splitting progressively decrease until $\delta = 1.8$ mm s^{-1} and $\Delta = 0.6$ mm s^{-1}, respectively. According to Eq. (7.28), the value $\delta = 1.8$ mm s^{-1} is characteristic of Li-rich Li_xSn alloys and shows that Sn atoms are mainly bonded to Li atoms. This is consistent with the small values of the quadrupole splitting that reflect rather symmetrical Sn environments.

From $x = 2.3$ to $x = 3.5$, both isomer shift and quadrupole splitting are almost constant, $\delta \approx 1.8$ mm s^{-1} and $\Delta \approx 0.6$ mm s^{-1}, showing there is no change in the local environment of the Sn atoms that are only surrounded by Li. The additional inserted Li atoms are expected to be located further from Sn atoms. This differs from the lithiation of βSn whose average isomer shift decreases continuously in the range $x = 0$–3.5 (Fig. 7.15). These different behaviors of βSn and a-$Si_{0.87}Sn_{0.13}$ can be related to the strong differences between the Sn local environments in the lithiated species. In lithiated $Li_xSi_{0.87}Sn_{0.13}$, the Sn atoms are tetrahedrally bonded to four first-nearest neighbors, whereas the Sn atoms in the Li_xSn alloys resulting from the lithiation of βSn are surrounded by more Li and Sn atoms. The variations of the Mössbauer parameters during the delithiation from $x = 3.5$ to $x = 1$ confirm the reversibility of the mechanism.

To conclude, the two successive sloping plateaus observed in the voltage curve of the lithiation of a-Si_ySn_{1-y} reflect the insertion of Li, first, close to Sn/Si atoms and then, close to Li atoms. This mechanism is reversible for delithiation.

7.5.5 βSn as Negative Electrode Material for Na-Ion Batteries

In contrast to Li-ion batteries, graphite cannot be used as negative electrode material for Na-ion batteries [104] and should be replaced by amorphous carbon. Tin could be an interesting alternative with a theoretical capacity of 850 mA h g^{-1} corresponding to the formation of $Na_{15}Sn_4$. However, the sodiation and desodiation of tin based

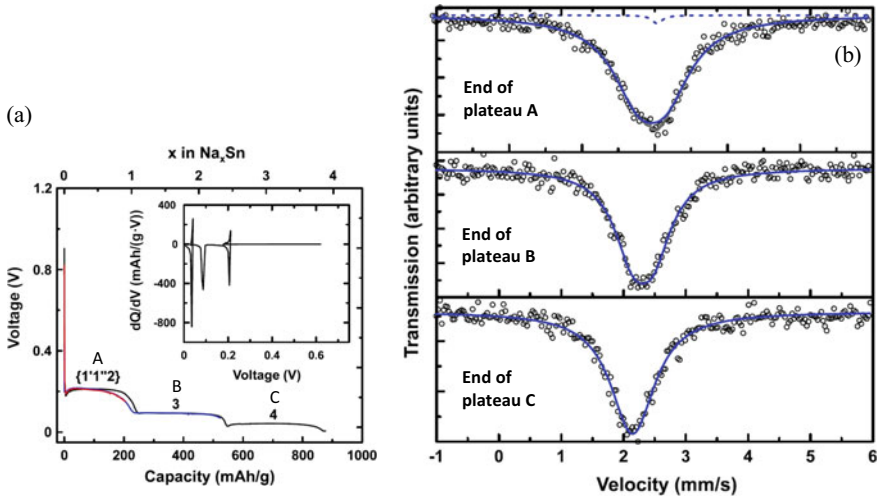

Fig. 7.18 **a** Voltage curves for the first sodiation of βSn in Na half-cells, showing three plateaus A, B and C at about 0.2 V, 0.1 V and 0.05 V. **b** Ex situ ^{119}Sn Mössbauer spectra recorded at the end of the plateaus A, B and C. Reprinted from Ref. [106]. Copyright 2014, with permission from Elsevier

electrodes also suffer from large volume variations as observed during the lithiation-delithiation cycles.

The voltage curve obtained for the first galvanostatic sodiation of βSn foil in a Na half-cell at low current rate shows three plateaus at about 0.2 V, 0.1 V and 0.05 V, respectively (Fig. 7.18a). These values are lower than those of the lithiation of βSn in a Li half-cell, in line with the difference between the standard electrode potentials of Li^+/Li (−3.04 V) and Na^+/Na (−2.71 V). The observed number of plateaus is lower than that expected from the formation of the eight equilibrium crystalline phases reported in the Na-Sn phase diagram [105].

The electrochemical reactions were characterized by ex situ ^{119}Sn Mössbauer spectroscopy, following the same approach as described for Li-ion batteries in Sect. 7.5.3 [106]. The room temperature spectra reported for crystalline NaSn, Na_9Sn_4 and $Na_{15}Sn_4$, and considered as reference materials, are all formed by a single peak. According to their number of Sn crystalline sites, the spectra of NaSn, Na_9Sn_4 and $Na_{15}Sn_4$ were successfully fitted to one doublet, two doublets and a single line, respectively. As observed for Li_xSn, the variations of the average isomer shift of Na_xSn, $\delta_{av}(x)$, can be used to distinguish Sn-rich from Na-rich Na_xSn phases. The isomer shift of NaSn (2.44 mm s^{-1}) is close to that of βSn, which corresponds to a Sn-rich Na_xSn phase. The isomer shifts of Na_9Sn_4 (2.3 mm s^{-1}) and $Na_{15}Sn_4$ (2.17 mm s^{-1}) are significantly lower than that of βSn and correspond to Na-rich Na_xSn phases. This behavior can be correlated to the number of Sn-Sn bonds as for Li_xSn. The isomer shifts of the Na_xSn phases are typical of Sn(0) oxidation state.

For a given value of x, the isomer shift of Na_xSn is higher than that of Li_xSn, which can be explained by the lower electronegativity of Na compared to Li.

The ex situ Mössbauer spectra obtained at the end of the three different voltage plateaus A, B and C are similar to those of NaSn, Na_9Sn_4 and $Na_{15}Sn_4$ reference materials, respectively (Fig. 7.18b). This indicates that the electrochemical sodiation of βSn at a very low Na rate leads to the formation of crystalline phases following the alloying reactions

$$\beta Sn + Na \rightarrow NaSn \tag{7.29}$$

$$2\,NaSn + 3\,Na \rightarrow Na_5Sn_2 \tag{7.30}$$

$$2\,Na_5Sn_2 + 5\,Na \rightarrow Na_{15}Sn_4 \tag{7.31}$$

Thus, the lithiation and sodiation of βSn in half-cells produce Li_xSn and Na_xSn crystalline phases, respectively, for $x < 2.5$. For $x > 2.5$, the formation of the $Na_{15}Sn_4$ equilibrium phase is observed instead of disordered Li-rich Li_xSn phases for lithiation. This could be due to differences in the diffusion of Li and Na atoms. The diffusion mechanisms could also explain the observed differences between the voltage profiles obtained for Sn foil and sputtered films in Na half-cells [107]. In the latter case, the mechanism is more complex, with the formation of Na_xSn amorphous and metastable phases. However, the ^{119}Sn Mössbauer spectrum of the fully sodiated electrode material is a single peak with the same Mössbauer isomer shift, $\delta = 2.14$ mm s^{-1}, as the $Na_{15}Sn_4$ reference crystalline phase. Further investigations on the phase transformations observed during the sodiation of βSn with other characterization tools led to somewhat different mechanisms but the fully sodiated phase is always $Na_{15}Sn_4$ [108–111]. This shows that, irrespective of the structure of the pristine material and the composition of the reaction intermediates, the same phase $Na_{15}Sn_4$ is obtained at the end of the sodiation of βSn, confirming the high capacity of this negative electrode material for Na-ion batteries. The observed different mechanisms suggest that, depending on the microstructure of the pristine material and the experimental conditions for electrochemical sodiation, the phase transformations can produce metastable and amorphous intermediate phases that differ from the crystalline references. For the lithiation of βSn, such a mechanism is mainly observed for Li-rich Li_xSn phases. This analysis shows that the electrochemical reactions taking place in βSn based negative electrodes of Li-ion or Na-ion batteries are rather complex due to both thermodynamic and kinetic effects. There are still some unclear aspects in these mechanisms that should be investigated by combining ^{119}Sn Mössbauer spectroscopy and other characterization tools.

7.6 Conversion Reactions

7.6.1 *$FeSn_2$ as Negative Electrode Material for Li-Ion Batteries*

Intermetallics composed of an electrochemically active element such as Si, Sn or Sb and an electrochemically inactive metallic element were investigated as negative electrode materials for Li-ion batteries in order to reduce the effects of the volume variations coming with alloying reactions [112–117]. Most of the tin based intermetallics, MSn_x, combine Sn with a transition metal element M that does not react with Li. The first lithiation is expected to extrude M from MSn_x to form metallic nanoparticles that maintain the dispersion of Li_xSn particles and improve the electronic conductivity. It is important to recall that the MSn_x active particles are mixed with carbon additives and a binder to form a porous film coated onto the current collector. The conductive additives play a key role in the performance of the electrodes during cycling. Carbon can also be introduced during the synthesis process to form MSn_x/C composites that were widely studied in the past in relation with the commercialization by Sony of the Nexelion Li-ion batteries [118–124]. $FeSn_2$ is regarded here as a typical example of the application of Mössbauer spectroscopy to MSn_x intermetallic based electrodes while other transition metals for M are briefly discussed in Sect. 7.6.2. $FeSn_2$ contains the highest amount of Sn among the crystalline phases reported in the Fe-Sn binary system, leading to the highest specific capacity as Fe-Sn based electrode material. Finally, $FeSn_2$ contains the two Mössbauer isotopes ^{57}Fe and ^{119}Sn to probe the electrochemical reactions at the atomic scale.

$FeSn_2$ has a tetragonal structure (*I*4/*mcm*) and each chemical element occupies one crystallographic site. Each Fe atom is at the center of a Sn square-based antiprism while Sn is bonded to four Fe atoms forming a $SnFe_4$ square-based pyramid. $FeSn_2$ is antiferromagnetic below 378 K [125]. Although the magnetic properties of $FeSn_2$ are not of real interest for electrochemical applications, they strongly affect the hyperfine structures, leading to rather complex and distinctive ^{57}Fe and ^{119}Sn Mössbauer spectra.

Crystalline microparticles of $FeSn_2$ were synthesized by solid-state reaction [126]. The ^{57}Fe Mössbauer spectrum of $FeSn_2$ at room temperature is formed by a sextet (Fig. 7.19a) while broad structures in the range 0–5 mm s^{-1} are observed for the ^{119}Sn Mössbauer spectrum (Fig. 7.19b), reflecting combined quadrupole effect and transferred hyperfine magnetic field [127]. The two sets of Mössbauer parameters: $\delta = 0.5$ mm s^{-1}, $\Delta = 0$ mm s^{-1} and $B = 11$ T for ^{57}Fe and $\delta = 2.18$ mm s^{-1}, $\Delta = 0.83$ mm s^{-1}, $B = 2.4$ T for ^{119}Sn are typical of Fe(0) and Sn(0) oxidation states, respectively, with a Sn asymmetrical environment.

The voltage profile obtained in galvanostatic regime at low current density consists of a low voltage plateau at 0.2 V for the first lithiation and voltage hystereses at the average value of 0.5 V for the subsequent delithiation-lithiation cycles [126]. This indicates that the first lithiation mechanism differs from the following reversible

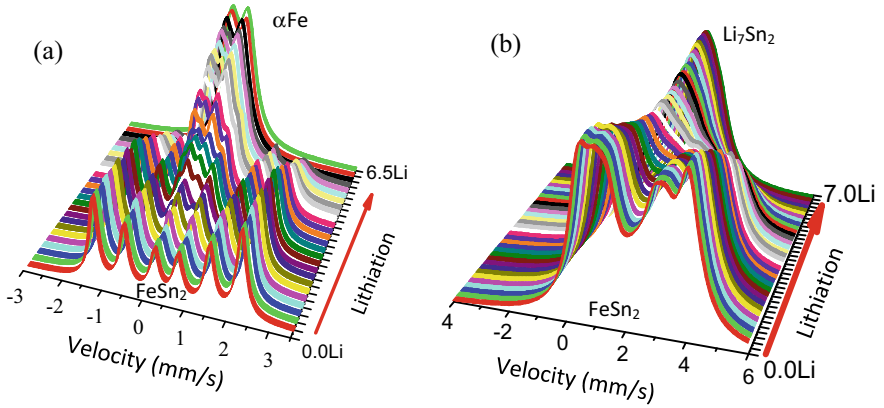

Fig. 7.19 Operando ^{57}Fe **a** and ^{119}Sn **b** Mössbauer spectra (fitted curves) obtained during the first lithiation of $FeSn_2$ in Cell 1

cycles and reflects a two-phase reaction. The operando XRD patterns show the progressive decrease of the intensity of the $FeSn_2$ Bragg peaks after the insertion of about 2 Li per $FeSn_2$ and the growth of broad peaks that can be assigned to Li-rich Li_xSn phases although the value of x cannot be determined. There are no Bragg peaks corresponding to Fe based phases.

The operando ^{119}Sn Mössbauer spectra collected during the first lithiation of $FeSn_2$ in Cell 1 show strong changes from a broadened magnetic spectrum to an asymmetrical peak at the end of the process (Fig. 7.19b). The latter spectrum was fitted to two doublets. The obtained isomer shifts of 1.88 and 1.98 mm s^{-1} are close to those of the Li_7Sn_2 crystalline reference but one quadrupole splitting, $\Delta =$ 0.72 mm s^{-1}, is smaller than the reference ($\Delta = 1.13$ mm s^{-1}). The DFT-LAPW evaluation of the Mössbauer parameters of the Li_7Sn_2 crystalline reference shows that the large quadrupole splitting originates from the Sn-Sn bond along the EFG principal axis Z for one of the two Sn crystallographic sites. For the other site, the quadrupole splitting is small due to the existence of only Li atoms as nearest neighbors. The observed experimental value, $\Delta = 0.72$ mm s^{-1}, for the fully lithiated electrode suggests that the number of Sn-Sn bonds in the electrochemically formed Li_7Sn_2 particles is lower than the reference. This could be due to the small size or the poor crystallinity of the particles. The contribution of the $FeSn_2$ sextet to the ^{57}Fe Mössbauer spectra decreases during the first lithiation while a doublet grows until the end of the process (Fig. 7.19a). The Mössbauer parameters of this doublet can be attributed to α-Fe nanoparticles in the paramagnetic state.

All the ^{57}Fe and ^{119}Sn Mössbauer spectra obtained during the first lithiation were successfully fitted to the spectra of $FeSn_2$/nano-αFe and $FeSn_2$/nano-Li_7Sn_2 phases, respectively. Since the number of atoms is constant in the in situ cell, the observed changes in the total area of the spectra correspond to the variations of the average recoil-free fraction. The total area of the ^{57}Fe Mössbauer spectra does not vary noticeably during lithiation, indicating that the ^{57}Fe recoil-free fractions of $FeSn_2$

and α-Fe have close values (Fig. 7.20a, inset). Thus, the relative amounts of $FeSn_2$ and α-Fe are directly given by their relative contributions to the ^{57}Fe Mössbauer spectra (Fig. 7.20a). The total area of the ^{119}Sn Mössbauer spectra is constant until 1 Li per $FeSn_2$ and then linearly decreases from 1 to 7 Li per $FeSn_2$ (Fig. 7.20b, inset). This can be related to the decrease of the average ^{119}Sn recoil-free fraction and shows that $f(FeSn_2) > f(Li_7Sn_2)$. By considering the full transformation of $FeSn_2$ into Li_7Sn_2 in the range 1–7 Li, one can determine the ratio $f(FeSn_2)/f(Li_7Sn_2) = 2.3$ from the slope of the regression line. The area of each ^{119}Sn Mössbauer subspectrum is proportional to the number of Sn atoms in the corresponding tin phase and to the ^{119}Sn recoil-free fraction (see Sect. 7.3.6). For $FeSn_2$ and Li_7Sn_2 that coexist during the first lithiation, the ratio between the ^{119}Sn recoil-free fractions of these two phases must be considered for an accurate evaluation of their relative amounts, transforming the non-linear variations of the relative areas of $FeSn_2$ and Li_7Sn_2 subspectra into linear variations for the relative amounts of $FeSn_2$ and Li_7Sn_2 (Fig. 7.20b).

The linear variations of the relative amounts of $FeSn_2$/α-Fe and $FeSn_2/Li_7Sn_2$ quantitatively show that the first lithiation of $FeSn_2$ can be assigned to the conversion reaction

$$FeSn_2 + 7\,Li \rightarrow Li_7Sn_2 + Fe \tag{7.32}$$

Additional information were obtained from magnetic measurements of the electrode material at different stages of lithiation. The saturation magnetization at low temperature of the fully lithiated electrode material is close to that of α-Fe. The ZFC/FC curves show the growth of a peak at 20 K with increasing number of Li that

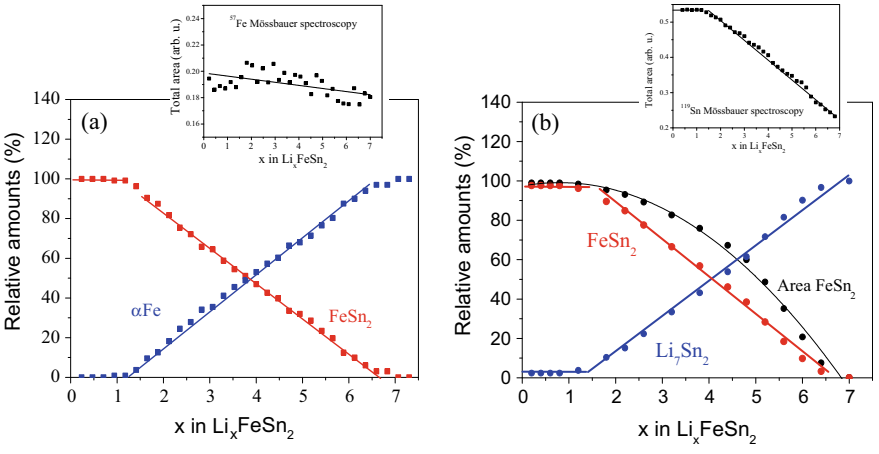

Fig. 7.20 First lithiation of $FeSn_2$ in Cell 1: **a** variations of the relative amounts of $FeSn_2$ (red) and α-Fe (blue) obtained from operando ^{57}Fe Mössbauer spectra and **b** variations of the relative amounts of $FeSn_2$ (red) and Li_7Sn_2 (blue) obtained from operando ^{119}Sn Mössbauer spectra. Total spectrum area vs. x in Li_xFeSn_2 (insets)

can be attributed to the progressive formation of superparamagnetic α-Fe nanoparticles with a constant average diameter of about 3 nm. This result is consistent with the extrusion of Fe atoms from $FeSn_2$ during the conversion reaction and the formation of α-Fe nanoparticles. The small size of the formed α-Fe particles explains the absence of XRD peaks. These results indicate that the first lithiation of $FeSn_2$ based electrodes should be considered as a restructuring step ending with the formation of α-Fe/Li_7Sn_2 nanocomposite, which is the real starting electrode material for the reversible lithiation-delithiation cycles.

Decreasing the particle size or increasing the surface area of electrochemically active materials are expected to improve the performance by enhancing the electrolyte impregnation, Li diffusion and electronic percolation. Nanostructured $FeSn_2$ particles were obtained by ball milling of $FeSn_2$ microparticles as confirmed by XRD showing broad Bragg peaks. The ^{57}Fe and ^{119}Sn Mössbauer spectra are formed by a single peak and a doublet, respectively, indicating the absence of hyperfine magnetic field as expected with the small size and poor crystallinity of the $FeSn_2$ ground particles [126]. However, the values of the isomer shift and quadrupole splitting are close to those of the antiferromagnetic $FeSn_2$ crystalline phase, showing that Fe and Sn local environments are similar in both nanostructured and crystalline $FeSn_2$. During the first lithiation, the voltage curve of nanostructured $FeSn_2$ decreases smoothly in contrast to the plateau observed for $FeSn_2$ microparticles, while ^{57}Fe and ^{119}Sn Mössbauer spectra both reflect the same conversion reaction as given by Eq. (7.32) [68]. Thus, nanostructured and crystalline $FeSn_2$ electrode materials are both transformed into an α-Fe/Li_7Sn_2 nanocomposite during the first lithiation.

The operando ^{119}Sn Mössbauer spectra obtained during the first delithiation of the $FeSn_2$ microparticle based electrode show the progressive transformation from a single peak into a broad doublet and the increase of the average isomer shift δ_{av} (Fig. 7.21a). The evolutions of the spectra and average isomer shift during the

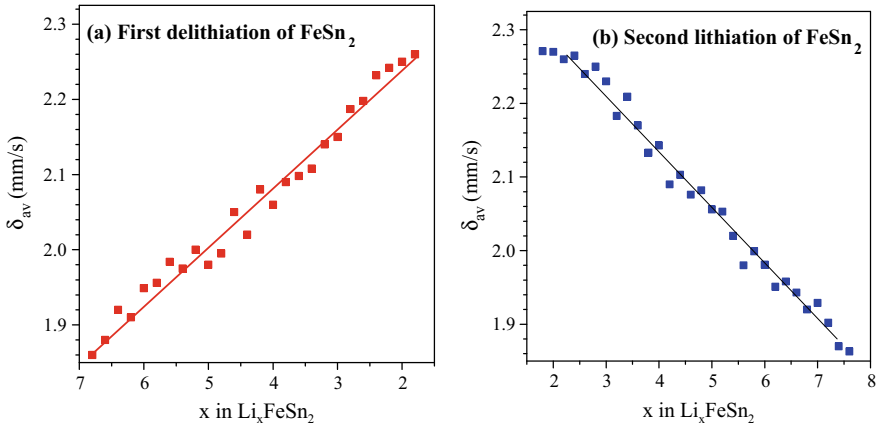

Fig. 7.21 Average experimental values of the ^{119}Sn Mössbauer isomer shift, δ_{av}, obtained during the first delithiation **a** and the second lithiation **b** of $FeSn_2$ in Cell 1

second lithiation are consistent with the reversibility of the mechanism observed during the first delithiation and strongly differs from the first lithiation (Fig. 7.21b). These spectra obtained for the first delithiation-lithiation reversible cycle cannot be unambiguously fitted by considering the Li_xSn references. However, the observed variations of δ_{av} in the range 1.8–2.3 mm s^{-1} can be interpreted from Eq. (7.28) as the variations of the Li_xSn average composition between Li_7Sn_2 and LiSn, which is consistent with the number of Li extracted during the first delithiation and inserted during the second lithiation.

A deeper delithiation can be obtained by decreasing the current density at the end of the process, leading to the back reaction of Fe with Sn extruded from Sn-rich Li_xSn and βSn to give $FeSn_2$ small particles [27]. However, for current densities commonly used in electrochemical tests, such a back reaction was not observed as confirmed by the ^{57}Fe Mössbauer spectra that do not change significantly during this first reversible cycle formed by the first delithiation and second lithiation. In that case, the reversible mechanism is based on alloying-dealloying Li-Sn reactions while α-Fe nanoparticles remain spectators and help to buffer the volume variations resulting from these reactions. The absence of back reaction between Fe and Sn during cycling was confirmed by electron paramagnetic resonance [128]. However, the existence of such reactions clearly depends on the experimental conditions used for the electrochemical tests.

7.6.2 Other Tin Based Intermetallic Compounds

The performance and electrochemical mechanisms of different tin based transition metal intermetallics were previously investigated, including $MnSn_2$ [129, 130], $CoSn_2$ [67, 131, 132], Ni_3Sn_4 [133–135] and Cu_6Sn_5 [136–139]. The voltage profiles obtained for the first three compounds are similar to that of $FeSn_2$. They are formed by a plateau for the first lithiation process and reversible voltage hystereses for the following delithiation-lithiation cycles. The main differences concern the voltage of the first-lithiation plateau and the existence of an additional plateau observed for some of these compounds at the end of delithiation. The ^{119}Sn Mössbauer spectra obtained during the first lithiation of $MnSn_2$, $CoSn_2$, and Ni_3Sn_4 based electrodes with similar galvanostatic regimes show the formation of Li_7Sn_2 according to the conversion reactions

$$MnSn_2 + 7\,Li \rightarrow Li_7Sn_2 + Mn \tag{7.33}$$

$$CoSn_2 + 7\,Li \rightarrow Li_7Sn_2 + Co \tag{7.34}$$

$$Ni_3Sn_4 + 14\,Li \rightarrow 2\,Li_7Sn_2 + 3\,Ni \tag{7.35}$$

The observed differences in the voltage values of the first lithiation plateau of $MnSn_2$, $CoSn_2$, and Ni_3Sn_4 can be mainly related to the enthalpies of the reactions (7.33)-(7.35) although significant kinetic effects can affect these values. In the three cases, the mechanisms of the first lithiation are the same as $FeSn_2$ and consist in the transformation of the pristine material into M/Li_7Sn_2 nanocomposite (M = Mn, Co, Ni). The Mössbauer spectra obtained at the end of the lithiation of $MnSn_2$, $CoSn_2$ and $FeSn_2$ are similar, reflecting the formation of poorly cristallized Li_7Sn_2 nanoparticles. For the fully lithiated Ni_3Sn_4 electrode, the Mössbauer spectrum is similar to that of the Li_7Sn_2 crystalline reference, suggesting the formation of a more stable phase.

Both $CoSn_2$ and $MnSn_2$ have the same *I*4/*mcm* structure as $FeSn_2$ while Ni_3Sn_4 has a monoclinic *C*2/*m* structure with two different Sn crystallographic sites in the primitive cell. $MnSn_2$ is antiferromagnetic below 325 K and the ^{119}Sn Mössbauer spectrum at room temperature was fitted to two sextuplets reflecting two Sn magnetic sites due to transferred hyperfine magnetic fields with parameters: $\delta = 2.34$ and 2.32 mm s^{-1}, $\Delta = 1.07$ and 1.10 mm s^{-1}, $B = 4.5$ and 2.7 T [140]. Nanostructured $MnSn_2$ was obtained by ball milling from crystalline $MnSn_2$. The Mössbauer spectrum is formed by a doublet showing the absence of transferred hyperfine magnetic field. The values of the Mössbauer parameters $\delta = 2.3$ mm s^{-1} and $\Delta = 1.1$ mm s^{-1} are close to those of crystalline $MnSn_2$ [129]. At room temperature, the Mössbauer spectrum of $CoSn_2$ can also be fitted to a doublet with $\delta = 2.14$ mm s^{-1}, $\Delta = 0.77$ mm s^{-1} [141].

These results show that the isomer shift slightly decreases for the series $MnSn_2$-$FeSn_2$-$CoSn_2$. According to Eq. (7.5), this reflects the decrease of the number of Sn 5s electrons and the increase of the number of Sn 5p electrons. In the latter case, this is due to electron transfer from the transition metal, M, to Sn through the Sn 5p–M 3d bonds. The decrease of the quadrupole splitting for this series reflects the decrease of the Sn 5p charge anisotropy. The Mössbauer spectrum of Ni_3Sn_4 is also formed by a doublet but was fitted by considering two Sn sites, in agreement with the crystal structure of this compound. The Mössbauer parameters are $\delta = 2.01$ mm s^{-1}, $\Delta = 0.7$ mm s^{-1} for one site and $\delta = 2.02$ mm s^{-1}, $\Delta = 1.18$ mm s^{-1} for the other site. The quadrupole splittings reflect the two different asymmetric environments of the Sn crystallographic sites [135]. It should be noted that different values of the average isomer shift of Ni_3Sn_4 can be found in the range ~1.9–2.1 mm s^{-1}, depending on the synthesis conditions. This reflects variations of the composition from Ni_3Sn_4 to $Ni_{3.5}Sn_4$ due to the existence of a solid solution [142]. In that case, Mössbauer spectroscopy can be used to evaluate the composition of $Ni_{3+x}Sn_4$ [143].

The values of the isomer shift decrease for the series $MnSn_2$-$FeSn_2$-$CoSn_2$-Ni_3Sn_4. This is due to changes in chemical bonds and electronic transfer, leading to the increase of the number of M 3d electrons. However, all the values are in the range 2.0–2.3 mm s^{-1}, which is typical of Sn(0) formal oxidation state (see Fig. 7.3). All these results explain why the first lithiation of nanostructured (paramagnetic) $MnSn_2$, nanostructured $FeSn_2$, $CoSn_2$ and Ni_3Sn_4, leads to similar changes in the ^{119}Sn Mössbauer spectra from a well-defined doublet for the pristine material to a slightly asymmetric doublet for Li_7Sn_2.

The mechanism is more complex for delithiation. The operando ^{119}Sn Mössbauer spectra obtained for the first delithiation of $CoSn_2$ [67] and nanostructured $MnSn_2$ based electrodes [130] show the same trends as $FeSn_2$. During the delithiation, the single Mössbauer peak of Li_7Sn_2 is broadened and transformed into a broadened doublet with increasing average isomer shift. This trend is typical of Li_7Sn_2 dealloying process. This suggests the formation of poorly crystallized Li_xSn nanoparticles with intermediate compositions as described in Sect. 7.6.1 for $FeSn_2$, or of more complex Li-Co-Sn and Li-Mn-Sn metastable ternary phases [130]. It is difficult to have a more reliable interpretation of the spectra since they do not show any resolved structures and the isomer shifts of the Sn based intermetallics and Li_xSn phases are all in the same range from 1.8 to 2.5 mm s^{-1}. The variations of the average isomer shift can be related to changes in the composition of the Li-Sn based species but it is impossible to identify well-defined phases as the Li_xSn crystalline references, which suggests the coexistence of metastable phases with possible different compositions, sizes and crystallinities, depending on the stage of delithiation.

For nanostructured $MnSn_2$, the voltage curve of the first delithiation shows an additional plateau at 0.75 V between about 2 and 3.5 Li per $MnSn_2$ (Fig. 7.22). Such an additional voltage plateau was also observed at the end of the delithiation of nanostructured $FeSn_2$ at very low current density and was interpreted as the back reaction of Fe with Sn to form small $FeSn_2$ particles [27]. However, the ^{119}Sn Mössbauer spectra obtained for $MnSn_2$ show a progressive line broadening with a shape typical of magnetic relaxations, which is not observed for $FeSn_2$ (Fig. 7.23). The spectra obtained for this additional plateau were successfully fitted to three doublets corresponding to remaining paramagnetic $MnSn_2$, the "Li-Mn-Sn" phase observed before this process and a magnetic subspectrum (Fig. 7.24). The latter doublet can be favourably compared to the spectrum obtained for crystalline $MnSn_2$ between room and Néel temperatures. This indicates that Sn reacts with Mn at the end of delithiation to form $MnSn_2$ with magnetic ordering although the $MnSn_2$ pristine material is paramagnetic. Such a magnetic ordering suggests that the reformation of $MnSn_2$ after the first cycle improves the crystallinity.

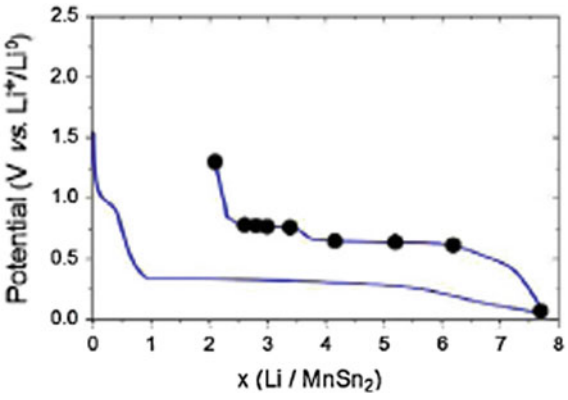

Fig. 7.22 Voltage curve for the first lithiation and delithiation of $MnSn_2$ in a Li half-cell. Reprinted from Ref. [130]. Copyright (2014), with permission from Elsevier

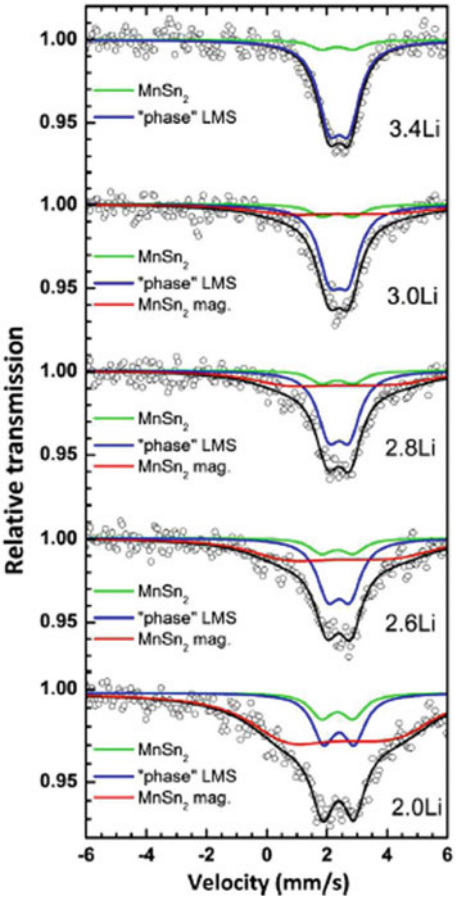

Fig. 7.23 Operando ^{119}Sn Mössbauer spectra obtained at the end of the delithiation of $MnSn_2$. Corresponding points are reported in Fig. 7.22. Reprinted from Ref. [130]. Copyright 2014, with permission from Elsevier

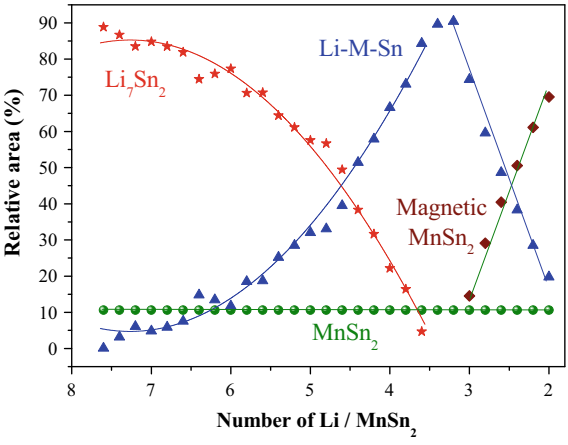

Fig. 7.24 Variations of the relative contributions to the ^{119}Sn Mössbauer spectra of the different Sn based phases formed during the first delithiation of $MnSn_2$ in a Li half-cell. Reprinted from Ref. [130]. Copyright 2014, with permission from Elsevier

For Ni_3Sn_4, the Mössbauer spectrum obtained at the end of delithiation is close to that of the pristine material and can be attributed to the reformation of Ni_3Sn_4. Such a back reaction was also observed for Ni_3Sn_4/Si/C composite where Si was introduced to increase the specific capacity [144]. In that case, both Ni_3Sn_4 and Si are electrochemically active and operando ^{119}Sn Mössbauer spectroscopy was used to follow reactions involving Sn. The spectra obtained in galvanostatic regime clearly show the back reaction of Ni with Sn to form Ni_3Sn_4 at the end of delithiation [145].

The present analysis of the Mössbauer results obtained for the first delithiation of tin intermetallics indicates that, depending on the transition metal M (Mn, Fe, Co, Ni), different mechanisms take place with different contributions of the back reactions between Sn and M. This could be due to differences in the bonding energies of M-Sn and M-M bonds, but also to interfacial and atomic diffusion properties. This aspect has not been elucidated yet and it is still not clear whether such back reactions that trap M and Sn atoms improve the electrode performance such as cycle life, which is a crucial issue for the application of intermetallic electrode materials in Li-ion batteries.

Finally, the Mössbauer spectra obtained during the second lithiation of $MnSn_2$, $CoSn_2$ and Ni_3Sn_4 differ from the spectra obtained during the first lithiation, in line with the observed different voltage profiles. This is consistent with the mechanism described for $FeSn_2$ and is obviously due to differences between the electrode materials at the beginning of the first (pristine) and second (nanocomposite) lithiations. However, both lithiation processes end with the formation of M/Li_7Sn_2 composite. The cycle formed by the first delithiation and the second lithiation is reversible and reflects the electrochemical mechanism (Li-Sn alloying reactions) of the following reversible cycles. Unfortunately, the poor mechanical stability of the electrodes during cycling limits the use of such materials and requires the optimization of the electrode formulation. In addition, all the reaction mechanisms described above can also be affected by parasitic reactions on cycling or for the cell at rest as discussed in the next subsection.

7.6.3 Aging Phenomena

Li-ion batteries can suffer from energy and power losses, voltage lowering or more severe issues with time. The performance degradation occurs for batteries at rest or during cycling [146]. The in situ Mössbauer spectroscopy can be used to study aging mechanisms if they affect the electronic properties of Mössbauer atoms. Two mechanisms are described here for tin based intermetallics as negative electrode materials for Li-ion batteries at rest and during cycling, respectively.

The first aging mechanism concerns the instability of the species formed during the lithiation or delithiation of electrode materials [147]. The example of a fully lithiated $FeSn_2$ based electrode is considered here. Such an aging process is complex since it depends not only on the macroscopic and microscopic features of the electrode as the morphology of the $FeSn_2$ particles or the electrode formulation, but also on

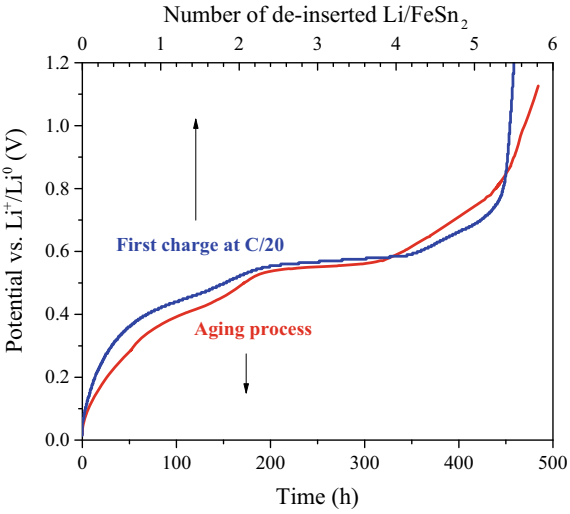

Fig. 7.25 Voltage curve of a fully lithiated $FeSn_2$ based electrode in a Li half-cell at rest as a function of time (red) compared to the galvanostatic voltage curve obtained for the first delithiation of $FeSn_2$ in a Li half-cell at the current rate of C/20 (0.05 Li per $FeSn_2$ and per hour). Reprinted with permission from Ref. [147]. Copyright 2017 American Chemical Society

the electrode-electrolyte reactivity. The present results highlight some trends in the instability of the nanocomposite α-Fe/Li_7Sn_2 formed at the end of the lithiation of $FeSn_2$ in a Li half-cell at rest, i.e., under open circuit conditions. In that case, the cell voltage increases with time from 0 to 1 V during a period of several months although there is no external current (Fig. 7.25). The observed voltage profile is similar to the profile of the galvanostatic delithiation of $FeSn_2$ in a Li half-cell, suggesting the progressive delithiation of Li_7Sn_2 with time.

The in situ ^{119}Sn Mössbauer spectra obtained during aging show that the rather symmetric peak of nano-Li_7Sn_2 centered at 2 mm s^{-1} is transformed into an asymmetric and broad line after 900 h (Fig. 7.26). The Mössbauer spectrum obtained after 170 h can be fitted to Li_7Sn_2 (2 doublets) and another doublet centered at 2.05 mm s^{-1}. The spectrum obtained after 900 h was fitted to two doublets centered at 2.05 mm s^{-1} and 2.45 mm s^{-1}, respectively. The average compositions of the formed Li_xSn phases were evaluated from Eq. (7.28). The values of the isomer shift $\delta = 2.05$ mm s^{-1} and $\delta = 2.45$ mm s^{-1} correspond to $Li_{2.5}Sn$ and $Li_{0.5}Sn$, respectively. Thus, the aging process consists in the delithiation of Li_7Sn_2 with the formation of intermediate Li_xSn phases as in the case of the galvanostatic delithiation process. The ^{57}Fe Mössbauer spectra do not show any noticeable changes even after three months, which means that iron nanoparticles were not affected by the delithiation of Li_7Sn_2. This was also confirmed by ex situ magnetic measurements [147].

The electrochemical impedance spectroscopy was also used for the characterization of the electrode-electrolyte interface [147]. Nyquist plots of the impedance spectra show two semicircles in medium and high frequency ranges attributed to charge transfer and SEI formation, respectively. During aging, the semicircles widened, revealing the increase of the resistances coming with these two phenomena. This was interpreted as the growth of the SEI layer and indicates that

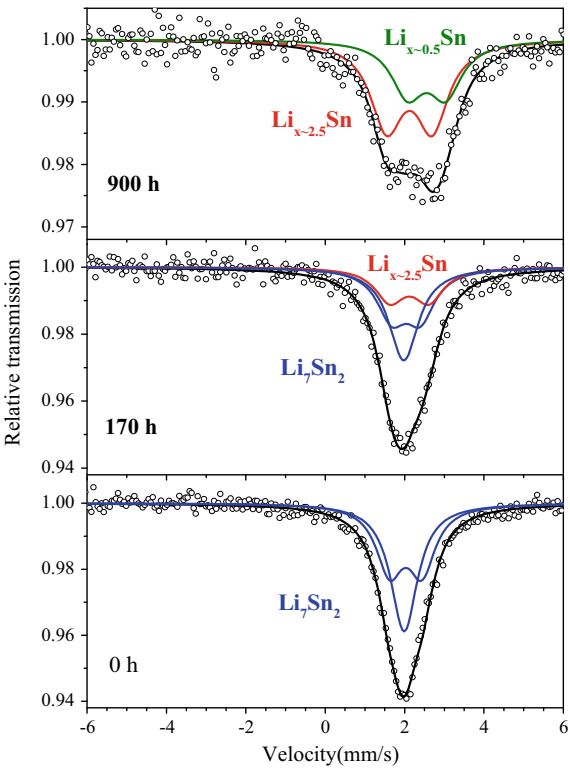

Fig. 7.26 In situ ^{119}Sn Mössbauer spectra at different stages of aging of a fully lithiated $FeSn_2$ electrode in a Li half-cell at rest. Reprinted with permission from Ref. [147]. Copyright 2017 American Chemical Society

the Li_7Sn_2 delithiation originates from reactions with the electrolyte. This is due to the metastability of the Li_xSn nanoparticles and their reactivity vs. Li.

Another aging process due to the metastability of the electrochemically formed species was revealed for delithiated $FeSn_2$ based electrodes in Li half-cells with voltage maintained during two weeks [27]. The delithiation of a fully lithiated $FeSn_2$ based electrode at very low current rate produces βSn, Sn-rich Li_xSn species and $FeSn_2$. When no more Li ions can be extracted from the electrode, and by imposing a constant voltage, the area of the Mössbauer spectrum increases with time. This can be interpreted by the increase of the amount of $FeSn_2$ in the electrode due to the back reaction of Sn with Fe.

The second aging phenomenon considered here occurs during cycling, leading to strong capacity fading [126]. The ^{57}Fe and ^{119}Sn Mössbauer spectra of a fully lithiated nanostructured $FeSn_2$ electrode obtained after 30–50 cycles show significant differences from the spectrum obtained at the end of the first lithiation.

The ^{57}Fe Mossbauer spectrum obtained after 30 cycles is formed by a magnetic sextet with the hyperfine magnetic field $B = 32.4$ T close to that of α-Fe and a single peak that can be attributed to superparamagnetic iron nanoparticles (Fig. 7.27a). The existence of magnetic particles can be explained by the growth of Fe nanoparticles during cycling. This is due to changes in the composite microstructure resulting from

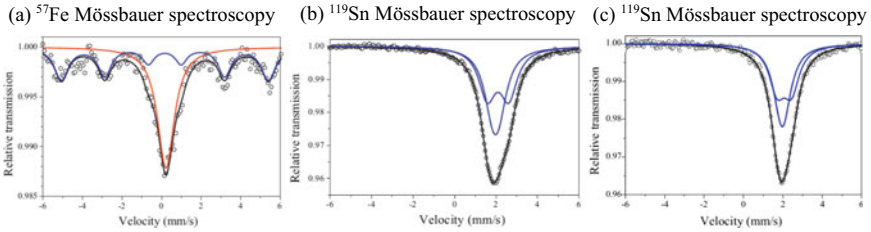

Fig. 7.27 ^{57}Fe **a** and ^{119}Sn **b** Mössbauer spectra of a fully lithiated $FeSn_2$ based electrode in a Li half-cell after 30 cycles and ^{119}Sn Mössbauer spectrum at the end of the first lithiation for comparison **c**. Reprinted with permission from Ref. [126]. Copyright 2011 from Elsevier

volume variations. The ^{119}Sn Mössbauer spectrum obtained after 30 cycles is more asymmetric than at the end of the first lithiation, but can also be fitted to two doublets (Fig. 7.27b). Compared to Li_7Sn_2 obtained at the end of the first lithiation (Fig. 7.27c), the highest of the two quadrupole splittings has increased by about 0.4 mm s^{-1} and the Mössbauer parameters are similar to those of the Li_7Sn_2 crystalline reference. Such a difference is explained in Sect. 7.6.1 and reflects here the growth of the Li_7Sn_2 particles during cycling.

The Mössbauer measurements show that the average particle size of the lithiation products α-Fe and Li_7Sn_2 increases on cycling, which reduces the electrochemical activity by worsening the effects of volume variations. The resulting mechanical, electrical and chemical instabilities are responsible for capacity fading. However, a longer cycle life can be achieved by improving the electrode microstructure and formulation.

7.6.4 Tin Oxides

Tin oxides and tin composite oxides (TCO) were proposed by Fuji in the late 1990s as high capacity negative electrode materials for Li-ion batteries [37]. The electrochemical mechanisms were studied by different techniques including operando XRD and ^{119}Sn Mössbauer spectroscopy.

The voltage curves of the first lithiation of SnO (Fig. 7.28) and SnO_2 in Li half-cells at low current density show two different regions. The region R1 corresponds to the insertion of about 2 Li per SnO (4 Li per SnO_2) and consists of a plateau at ≈ 1 V (SnO_2 ≈ 1.5 V). The region R2 shows a continuous voltage decrease with different sloping plateaus until the end of lithiation. The voltage curve in R2 depends on the imposed current and can change from smooth to staircase profile with decreasing current, reflecting the effect of reaction kinetics as observed for βSn.

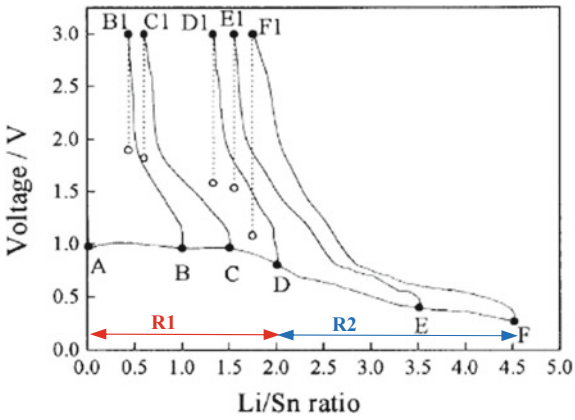

Fig. 7.28 Voltage curves of SnO in Li half-cells with the points of measurements for the first lithiation (A-F) and for different stages of delithiation at 3 V (B1-F1). Two regions R1 and R2 are distinguished for lithiation. Reprinted from Ref. [148]. Copyright 2000, with permission from Elsevier

The electrochemical reactions of SnO in Li half-cells were studied by operando [149] and ex situ [148] ^{119}Sn Mössbauer spectroscopy. The experimental conditions are different in the two works but the observed trends in the evolution of the Mössbauer spectra are similar.

For ex situ experiments, the Mössbauer spectrum of SnO formed by an asymmetric doublet centered at 2.6 mm s^{-1} is progressively broadened at the low velocity side and the doublet disappears to form a large and unresolved structure at the end of R1 (A-D in Fig. 7.29). The spectra were fitted to three components corresponding to SnO, βSn and Sn(IV) oxides, respectively, and an additional component centered at about 1.2 mm s^{-1}. The contribution of SnO to the Mössbauer spectra decreases while the contributions of βSn and the component centered at 1.2 mm s^{-1} increase during lithiation. For in situ experiments, only the Mössbauer spectra at the beginning and at the end of R1 were reported and are similar to the corresponding ex situ spectra [149]. These two studies are consistent with the transformation of SnO into βSn in R1, which corresponds to the conversion reaction

$$\mathrm{SnO} + 2\,\mathrm{Li} \rightarrow \beta\mathrm{Sn} + \mathrm{Li_2O} \tag{7.36}$$

However, the existence of the other two Mössbauer subspectra indicates that the mechanism is not a simple conversion reaction leading to isolated βSn and Li_2O particles. The observed Mössbauer isomer shift of the Sn(IV) oxide is slightly higher than that of SnO_2 and could originate from surface oxidation or impurities. The other subspectrum at 1.2 mm s^{-1} is rather intriguing since this value cannot be assigned to either Sn(IV) oxides nor Sn(0) phases (see Fig. 7.3). It can be tentatively attributed to Sn bonded to both Sn and O atoms resulting from interactions between βSn and Li_2O particles or to metastable Li-Sn-O amorphous phases. The reported variations of the total area of the operando Mössbauer spectra as a function of the number of Li per SnO, x, can be related to the variations of the average recoil-free fraction since the total amount of Sn is constant in the cell [149]. As a main result, the recoil-free fraction decreases almost linearly with increasing x and the ratio $f(x = 0)/f(x =$

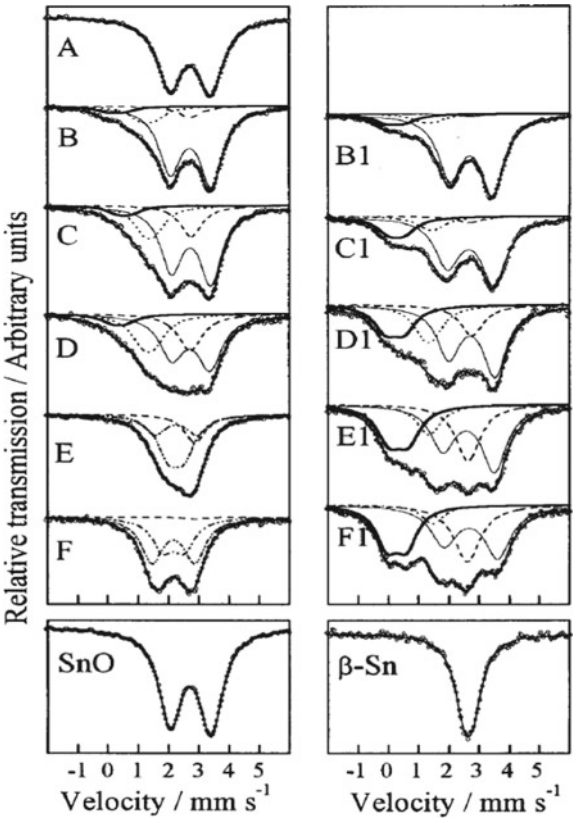

Fig. 7.29 Ex situ ^{119}Sn Mössbauer spectra at different stages of the first lithiation (A-F) and delithiation (B1-F1) of SnO in Li half-cells. The different subspectra correspond to Sn(IV) oxide (bold solid line), SnO (solid line), Li-Sn-O (dotted line), βSn (dashed line) and Li_xSn (dash-dotted line). Corresponding points are reported in Fig. 7.28. The spectra of SnO and βSn are shown for comparison. Reprinted from Ref. [148]. Copyright 2000, with permission from Elsevier

2) can be compared to $f(\text{SnO})/f(\beta\text{Sn})$, which confirms the conversion reaction given by Eq. (7.36). Thus, the lithiation of SnO in R1 brings about the dispersion of small Sn(0) electrochemically active particles within an inactive Li_2O based matrix, which should be regarded as an in situ restructuring step of the electrode material.

The operando Mössbauer spectra obtained during the lithiation in R2 are similar to those of the Li_xSn reference materials, which suggests the formation of Li_xSn equilibrium phases [149]. For Li_2Sn_5 and LiSn, there is still a low velocity component due to remaining Sn-O bonds. The agreement between the experimental data and Li_xSn references is less clear for compositions around Li_5Sn_2, probably due to the existence of different and metastable phases, while Li_7Sn_2 and $Li_{22}Sn_5$ are clearly observed at the end of R2. The latter result differs from the lithiation of βSn based electrodes that shows more disordered Li-rich Li_xSn phases as discussed in Sect. 7.5.2. This could be due to the effect of the Li_2O matrix that improves the dispersion of the Li_xSn small particles and the formation of more ordered phases.

The operando Mössbauer spectra obtained during the delithiation are similar to the Li_xSn references until LiSn [149]. Then, additional extraction of Li leads to broadened spectra at the low velocity side as voltage increases above 1 V. This can

be explained by the formation of Sn-O bonds. Since all the Li atoms are extracted from Li_xSn at this stage, this is due to the partial delithiation of Li_2O and back reaction of Sn with O. The in situ spectrum obtained for the delithiated electrode at 2.5 V shows the existence of SnO_2, SnO and βSn, confirming such a back reaction. The same results are obtained for ex situ measurements at 3 V (Fig. 7.29) [148]. These reactions operate at a rather high voltage and are not expected to occur for SnO based negative electrodes in Li-ion full-cells.

To summarize, the electrochemical mechanism of SnO in a Li half-cell consists in the irreversible transformation of Sn(II)O into βSn(0) and Li_2O small particles, followed by reversible Li_xSn alloying and dealloying reactions for the first delithiation and the second lithiation, respectively, if the upper voltage cutoff is limited to about 1 V. In that case, the Li_2O particles form an electrochemically inactive matrix that maintains the dispersion of the Li_xSn particles, improving the cycling properties of the electrode compared to βSn. This is the same basic concept as described in Sect. 7.6.1 for tin intermetallic based electrodes whose metallic nanoparticles formed during the first lithiation buffer the volume variations, as the Li_2O particles in the present case. However, there is a large capacity loss at first cycle due to the transformation of SnO into $\beta Sn/Li_2O$. In Li-ion full-cells, such a reaction requires the prelithiation of the negative electrode or the increase of the positive/negative electrode ratio.

The situation is even more critical for SnO_2 since 4 Li per SnO_2 are required for the conversion reaction ending with $\beta Sn/Li_2O$ composite. The in situ ^{119}Sn Mössbauer spectroscopy was used for SnO_2 in a plastic bag half-cell showing a three-step mechanism for the first lithiation including intercalation, conversion and alloying reactions [150]. However, the analysis of the conversion reaction is more ambiguous due to overlaps between the Sn(IV)O_2 subspectrum and broad lines due to the Sn-O bonds between βSn and Li_2O. The additional initial step reflecting Li intercalation into SnO_2 only involves 0.4 Li per SnO_2. The voltage curve of SnO_2 corresponding to Li_xSn alloying reactions (R2 for SnO) does not show well-defined plateaus and the Mössbauer spectra cannot be fitted to Li_xSn references. However, the variations of the average isomer shift are linear in this region, as expected from Eq. (7.28), reflecting reversible Li_xSn alloying reactions.

As an example of TCO, a tin borophosphate glass with the composition Sn_2BPO_6 is considered here since the mechanism was studied by operando ^{119}Sn Mössbauer spectroscopy [149]. The voltage profile of the first cycle of Sn_2BPO_6 in a Li half-cell is similar to that of SnO, except that the first plateau (R1) has a higher voltage. The Mössbauer spectrum of the pristine material consists of an asymmetric doublet that can be attributed to Sn(II) while a broad spectrum of weak intensity was obtained at the end of the first plateau. This reflects the strong decrease of the average recoil-free fraction in R1, which was attributed to the transformation of Sn_2BPO_6 into βSn small clusters embedded in a mixed borophosphate and Li_2O matrix. Such a decrease can be related to the variations of the recoil-free fraction of βSn as particle size decreases below ~10 nm when the interface with the matrix is not too constrained [149]. The proposed conversion reaction is

$$2\ Sn_2BPO_6 + 8Li \rightarrow 4\beta Sn + B_2O_3 + P_2O_5 + 4\ Li_2O \tag{7.37}$$

The Mössbauer absorption increases during the lithiation in R2 and the spectra are typical of the Li_xSn references except around Li_5Sn_2 [149]. The Mössbauer spectra obtained during the delithiation until about 1 V are similar to those obtained during the lithiation in R2 but in reverse order, ending with βSn. This shows that Li_xSn alloying reactions are reversible in R2. The spectrum of the delithiated electrode at the higher voltage of 2.5 V was successfully fitted to βSn and Sn_2BPO_6, suggesting back reactions of Sn with the oxides to form species with similar Sn local environments as the pristine glass. Thus, the electrochemical mechanism of Sn_2BPO_6 glass is similar to that of SnO except that the Sn(0) particles obtained during the initial conversion reaction given by Eq. (7.37) are significantly smaller and embedded in a more complex matrix. The small size of the βSn clusters reduces the impact of volume variations and the borophosphate matrix is more efficient to maintain the particle dispersion, which improves the cyclability of Sn_2BPO_6 glass compared to βSn. Finally, it should be noted that the upper voltage cutoff (≈ 0.8 V) is an important parameter to avoid the aggregation of mobile βSn clusters and the instability of the oxide based matrix due to back reactions between Sn and O atoms.

7.7 Conclusions

Mössbauer spectroscopy is a powerful tool to characterize pristine electrode materials and investigate reaction mechanisms in Li-ion and Na-ion batteries. This is due to the ability of this technique to probe the local environment of nuclei due its high selectivity to detect weak variations of the nuclear energy levels arising from electric and magnetic interactions. The resulting Mössbauer parameters: isomer shift, quadrupole splitting and hyperfine magnetic field, combined with the recoil-free fraction and the spectral linewidth, provide information about the structural, electronic and magnetic properties of electrode materials.

Changes in the Mössbauer parameters due to insertion and deinsertion processes can be used to follow electrochemical reactions. Although the application of Mössbauer spectroscopy could be limited due to the small number of available isotopes, the two most commonly used ones, ^{57}Fe and ^{119}Sn, are fortunately often found in the composition of electrode materials or they can be introduced as local probes. In situ and operando measurements are of high interest for the analysis of reaction mechanisms on a real-time basis and different types of in situ electrochemical cells have been described. Such cells avoid extracting the rather unstable lithiated or sodiated electrode materials although ex situ experiments can also be achieved if sample handling and measurements are made with care and shortly after the electrochemical experiments.

Some selected examples have been considered to illustrate the three main mechanisms encountered in electrode materials: insertion, alloying and conversion. These reactions can be characterized from changes in the oxidation state of the Mössbauer

atoms due to redox reactions, but also from modifications in chemical bonding and local structure. Mössbauer spectroscopy is also of high interest for the identification and the quantitative evaluation of the lithiated or sodiated products. However, it should be emphasized that Mössbauer spectroscopy should be combined with other characterization tools to explore both short-range and long-range interactions, providing more accurate and quantitative analyses.

The interpretation of Mössbauer spectra is often complex due to the existence of a large variety of local environments in the electrochemically formed species. A particular attention should be devoted to the Mössbauer data analysis that can take advantages of first-principles calculations. Such calculations should also be used to investigate the structures of the lithiated or sodiated phases that are often metastable. This could be of high interest for the analysis of kinetic effects in Li-ion and Na-ion batteries, which are usually not taken into account in the interpretation of the Mössbauer experiments. The use of synchrotron radiation could also be considered for such phenomena in order to reduce the acquisition time of spectra.

However, in-lab Mössbauer spectroscopy will undoubtedly make novel contributions in the future to the development of new materials for electrochemical energy storage, which will be crucial for the energy transition and the reduction of global warming.

Acknowledgements The author is grateful to all collaborators and students who have contributed to the studies of Li-ion and Na-ion batteries, and in particular, J. C. Jumas, J. Olivier-Fourcade, M. T. Sougrati, M. Womes, L. Aldon, C. Bousquet, M. Chamas, J. Chouvin, R. Dedryvère, S. Difi, Y. He, M. El Khalifi, A. Mahmoud, M. Mouyane, S. Naille, A. Perea and F. Robert.

References

1. M. Armand, J.M. Tarascon, Nature **451**, 652 (2008)
2. B. Dunn, H. Kamath, J.-M. Tarascon, Science **334**, 928 (2011)
3. J. Jaguemont, L. Boulon, Y. Dubé, Appl. Energy **164**, 99 (2016)
4. A. Opitz, P. Badami, L. Shen, K. Vignarooban, A.M. Kannan, Renew. Sustain. Energy Rev. **68**, 685 (2017)
5. M. Winter, B. Barnett, K. Xu, Chem. Rev. **118**, 11433 (2018)
6. D. Aurbach, E. Zinigrad, Y. Cohen, H. Teller, Solid State Ionics **148**, 405 (2002)
7. C. Sun, J. Liu, Y. Gong, D.P. Wilkinson, J. Zhang, Nano Energy **33**, 363 (2017)
8. F. Zheng, M. Kotobuki, S. Song, M.O. Lai, L. Lu, J. Power Sources **389**, 198 (2018)
9. W. Xu, J. Wang, F. Ding, X. Chen, E. Nasybulin, Y. Zhang, J.-G. Zhang, Energy Environ. Sci. **7**, 513 (2014)
10. J.B. Goodenough, K.-S. Park, J. Am. Chem. Soc. **135**, 1167 (2013)
11. V. Etacheri, R. Marom, R. Elazari, G. Salitra, D. Aurbach, Energy Environ. Sci. **4**, 3243 (2011)
12. N. Nitta, F. Wu, J.T. Lee, G. Yushin, Mater. Today **18**, 252 (2015)
13. P. Rozier, J.M. Tarascon, J. Electrochem. Soc. **162**, A2490 (2015)
14. M. Yoshido, R.J. Brodd, A. Kozawa, *Li-Ion Batteries* (Springer, New York, 2009)
15. J.B. Goodenough, Y. Kim, Chem. Mater. **22**, 587 (2010)
16. G.E. Blomgren, J. Electrochem. Soc. **164**, A5019 (2017)
17. A. Barai, K. Uddin, M. Dubarry, L. Somerville, A. McGordon, P. Jennings, I. Bloom, Progr. Energy Combust. Sci. **72**, 1 (2019)

18. Z. Shadike, E. Zhao, Y.-N. Zhou, X. Yu, Y. Yang, E. Hu, S. Bak, L. Gu, X.Q. Yang, Advan. Energy Mater. **8**, 1702588 (2018)
19. R. Dedryvère, S. Leroy, H. Martinez, F. Blanchard, D. Lemordant, D. Gonbeau, J. Phys. Chem. B **110**, 12986 (2006)
20. G. Kermani, E. Sahraei, Energies **10**, 1730 (2017)
21. P. Novák, J.C. Panitz, F. Joho, M. Lanz, R. Imhof, M. Coluccia, J. Power Sources **90**, 52 (2000)
22. X. Ma, W. Luo, M. Yan, L. He, L. Mai, Nano Energy **24**, 165 (2016)
23. P.P.R.M.L. Harks, F.M. Mulder, P.H.L. Notten, J. Power Sources **288**, 92 (2015)
24. P.E. Lippens, L. Aldon, C.M. Ionica, F. Robert, J. Olivier-Fourcade, J.C. Jumas, in *Solid State Ionics-2004*, ed. by P. Knauth et al. (2005), p. 249
25. P.E. Lippens, M.E. Khalifi, M. Chamas, A. Perea, M.-T. Sougrati, C. Ionica-Bousquet, L. Aldon, J. Olivier-Fourcade, J.-C. Jumas, in *ICAME 2011: Proceedings of the 31st International Conference on the Applications of the Mössbauer Effect (ICAME 2011) held in Tokyo, Japan, 25–30 September 2011*, ed. by Y. Yoshida (Springer Netherlands, Dordrecht, 2013), p. 331.
26. P.E. Lippens, J.C. Jumas in *Nanocomposites: Ionic Conducting Materials and Structural Spectroscopies*, ed. by P. Knauth, J. Schoonman (Springer New York, 2008), p. 247
27. R.A. Dunlap, O. Mao, J.R. Dahn, Phys. Rev. B **59**, 3494 (1999)
28. F. Berry, in *Mössbauer Spectroscopy Applied to Inorganic Chemistry*, vol.1, ed. by G.J. Long (Plenum Press, New York and London, 1984), p. 391
29. C.M. Ionica, P.E. Lippens, J.O. Fourcade, J.C. Jumas, J. Power Sources **146**, 478 (2005)
30. B. Mortemard de Boisse et al., Nat. Commun. **7**, 11397 (2016)
31. L. Aldon, P. Kubiak, A. Picard, J.C. Jumas, J. Olivier-Fourcade, Chem. Mater. **18**, 1401 (2006)
32. M. Van Thournout, L. Aldon, M. Womes, B. Ducourant, J. Olivier-Fourcade, C. Tessier, S. Levasseur, J. Power Sources **174**, 1270 (2007)
33. J.M. Tarascon, M. Armand, Nature **414**, 359 (2001)
34. M. Endo, C. Kim, K. Nishimura, T. Fujino, K. Miyashita, Carbon **38**, 183 (2000)
35. Y.P. Wu, E. Rahm, R. Holze, J. Power Sources **114**, 228 (2003)
36. E. Buiel, J.R. Dahn, Electrochim. Acta **45**, 121 (1999)
37. Y. Idota, T. Kubota, A. Matsufuji, Y. Maekawa, T. Miyasaka, Science **276**, 1395 (1997)
38. Sony's new Nexelion hybrid lithium ion batteries to have thirty-percent more capacity than conventionl offering: www.sony.net/SonyInfo/News/Press/200502/05-006E/
39. T.C. Gibb, *Priciples of Mössbauer Spectroscopy* (Chapman and Hall Ltd., London, 1976)
40. G.J. Long, *Mössbauer spectroscopy applied to inorganic chemistry*, vol. 1, (Plenum Press, New York, 1984), Modern Inorganic Chemistry
41. D.P.E. Dickson, F. Berry, *Mössabauer Spectroscopy* (Cambridge University Press, Cambridge, 1986)
42. Y. Yoshida, G. Langouche, *Mössbauer Spectroscopy* (Springer-Verlag, Berlin Heidelberg, 2013)
43. T. Segi, R. Masuda, Y. Kobayashi, T. Tsubota, Y. Yoda, M. Seto, Hyperfine Interact. **237**, 7 (2016)
44. F. Neese, Inorg. Chim. Acta **337**, 181 (2002)
45. A.M. Mudarra Navarro, C.E. R. Torres, L.A. Errico, Hyperfine Interact. **202**, 117 (2011)
46. M. El Khalifi, P.E. Lippens, J. Phys. Chem. C **120**, 28375 (2016)
47. P.E. Lippens, M. El Khalifi, M. Womes, Physica Status Solidi (B) **254**, 1600194 (2017)
48. A. Svane, N.E. Christensen, C.O. Rodriguez, M. Methfessel, Phys. Rev. B **55**, 12572 (1997)
49. U.D. Wdowik, K. Ruebenbauer, Phys. Rev. B **76**, 155118 (2007)
50. K.S.P. Blaha, G.K.H. Madsen, D. Kvasnicka, J. Luitz, (2001. ISBN 3-9501031-1-2)
51. G.K. Shenoy, W.F.E., *Mössbauer isomer shift* (North-Holland Publishing Company, Amsterdam, Oxford, New York, 1978)
52. G.K. Shenoy, in *Mössbauer Spectroscopy applied to Inorganic Chemistry* ed. by G.J. Long (Plenum Press, New York and London, 1984), p. 57

53. R.V. Parish, in *Mössbauer spectroscopy* ed. by D.P.E. Dickson, F.J. Berry (Cambridge University Press, Cambridge, 1986), p. 17
54. P.E. Lippens, Phys. Rev. B **60**, 4576 (1999)
55. H. Spiering, in *Mössbauer Spectroscopy Applied to Inorganic Chemistry*. ed. by G.J. Long (Plenum Press, New York and London, 1984), p. 79
56. P. Dufek, P. Blaha, K. Schwarz, Phys. Rev. Lett. **75**, 3545 (1995)
57. P.E. Lippens, J. Olivier-Fourcade, J.C. Jumas, Hyperfine Interact. **126**, 137 (2000)
58. A. Svane, Phys. Rev. B **68**, 064422 (2003)
59. H. Haas, M. Menningen, H. Andreasen, S. Damgaard, H. Grann, F.T. Pedersen, J.W. Petersen, G. Weyer, Hyperfine Interact. **15**, 215 (1983)
60. P.E. Lippens, J.C. Jumas, J. Olivier-Fourcade, Hyperfine Interact. **141**, 303 (2002)
61. R. Ingalls, Phys. Rev. **128**, 1155 (1962)
62. C. Hohenemser, Phys. Rev. **139**, A185 (1965)
63. H.D. Pfannes, U. Gonser, Appl. Phys. **1**, 93 (1973)
64. R.A. Dunlap, M.N. Obrovac, J. Li, A. Smith, T.D. Hatchard, R.J. Sanderson, J.R. Dahn, Mössbauer Eff. Ref. Data J. **33**, 37 (2010)
65. A. Wattiaux, L. Fournès, C. Delmas, Mössbauer Eff. Ref. Data J. **33**, 32 (2010)
66. K. Ariyoshi, T. Ohzuku, Mössbauer Eff. Ref. Data J. **33**, 43 (2010)
67. C.M. Ionica-Bousquet, P.E. Lippens, L. Aldon, J. Olivier-Fourcade, J.C. Jumas, Chem. Mater. **18**, 6442 (2006)
68. M. Chamas, M.T. Sougrati, C. Reibel, P.E. Lippens, Chem. Mater. **25**, 2410 (2013)
69. J.B. Leriche et al., J. Electrochem. Soc. **157**, A606 (2010)
70. J.C. Jumas et al., Patent FR2995081A1, WO2014033402A1 (2014)
71. S. Difi, I. Saadoune, M.T. Sougrati, R. Hakkou, K. Edstrom, P.E. Lippens, J. Phys. Chem. C (2015)
72. S. Difi, I. Saadoune, M.T. Sougrati, R. Hakkou, K. Edstrom, P.E. Lippens, Hyperfine Interact. **237**, 61 (2016)
73. C. Delmas, F. Cherkaoui, A. Nadiri, P. Hagenmuller, Mater. Res. Bull. **22**, 631 (1987)
74. A. Mahmoud, C. Karegeya, M.T. Sougrati, J. Bodart, B. Vertruyen, R. Cloots, P.E. Lippens, F. Boschini, A.C.S. Appl, Mater. Interfaces **10**, 34202 (2018)
75. A. Perea, M.T. Sougrati, C.M. Ionica-Bousquet, B. Fraisse, C. Tessier, L. Aldon, J.C. Jumas, RSC Advan. **2**, 2080 (2012)
76. M. Ati, M.T. Sougrati, G. Rousse, N. Recham, M.L. Doublet, J.C. Jumas, J.M. Tarascon, Chem. Mater. **24**, 1472 (2012)
77. A. Yamada, N. Iwane, S.-I. Nishimura, Y. Koyama, I. Tanaka, J. Mater. Chem. **21**, 10690 (2011)
78. B. Mortemard de Boisse et al., J. Mater. Chem. A **3**, 10976 (2015)
79. A. Blidberg, L. Häggström, T. Ericsson, C. Tengstedt, T. Gustafsson, F. Björefors, Chem. Mater. **27**, 3801 (2015)
80. G. Rousse, J. Rodriguez-Carvajal, S. Patoux, C. Masquelier, Chem. Mater. **15**, 4082 (2003)
81. A.S. Andersson, B. Kalska, L. Häggström, J.O. Thomas, Solid State Ionics **130**, 41 (2000)
82. L. Aldon, A. Perea, M. Womes, C.M. Ionica-Bousquet, J.C. Jumas, J. Solid State Chem. **183**, 218 (2010)
83. P.E. Lippens, M. El Khalifi, M. Chamas, A. Perea, M.T. Sougrati, C. Ionica-Bousquet, L. Aldon, J. Olivier-Fourcade, J.C. Jumas, Hyperfine Interact. **206**, 35 (2012)
84. A. Perea, M.T. Sougrati, C.M. Ionica-Bousquet, B. Fraisse, C. Tessier, L. Aldon, J.C. Jumas, RSC Advances **2**, 9517 (2012)
85. N. Recham, G. Rousse, M.T. Sougrati, J.-N. Chotard, C. Frayret, S. Mariyappan, B.C. Melot, J.-C. Jumas, J.M. Tarascon, Chem. Mater. **24**, 4363 (2012)
86. R. Amisse, M.T. Sougrati, L. Stievano, C. Davoisne, G. Dražič, B. Budič, R. Dominko, C. Masquelier, Chem. Mater. **27**, 4261 (2015)
87. H. Ahouari, G. Rousse, J. Rodríguez-Carvajal, M.-T. Sougrati, M. Saubanère, M. Courty, N. Recham, J.M. Tarascon, Chem. Mater. **27**, 1631 (2015)

88. A. Nytén, S. Kamali, L. Häggström, T. Gustafsson, J.O. Thomas, J. Mater. Chem. **16**, 2266 (2006)
89. M.N. Obrovac, V.L. Chevrier, Chem. Rev. **114**, 11444 (2014)
90. I.A. Courtney, J.S. Tse, O. Mao, J. Hafner, J.R. Dahn, Phys. Rev. B **58**, 15583 (1998)
91. J. Sangster, C.W. Bale, J. Phase Equilib. **19**, 70 (1998)
92. C. Lupu, J.G. Mao, J.W. Rabalais, A.M. Guloy, J.W. Richardson, Inorg. Chem. **42**, 3765 (2003)
93. W. Gasior, Z. Moser, W. Zakulski, J. Non-Cryst, Solids **205–207**, 379 (1996)
94. R. Sen, P. Johari, A.C.S. Appl, Mater. Interfaces **9**, 40197 (2017)
95. M. Mayo, A.J. Morris, Chem. Mater. **29**, 5787 (2017)
96. M. Mayo, J.P. Darby, M.L. Evans, J.R. Nelson, A.J. Morris, Chem. Mater. (2018)
97. R.A. Dunlap, D.A. Small, D.D. MacNeil, M.N. Obrovac, J.R. Dahn, J. Alloys Compd. **289**, 135 (1999)
98. F. Robert, P.E. Lippens, J. Olivier-Foureade, J.C. Jumas, F. Gillot, M. Morcrette, J.M. Tarascon, J. Solid State Chem. **180**, 339 (2007)
99. S. Naille, J.C. Jumas, P.E. Lippens, J. Olivier-Fourcade, J. Power Sources **189**, 814 (2009)
100. J. Chouvin, J. Olivier-Fourcade, J.C. Jumas, B. Simon, O. Godiveau, Chem. Phys. Lett. **308**, 413 (1999)
101. J. Li, A. Smith, R.J. Sanderson, T.D. Hatchard, R.A. Dunlap, J.R. Dahn, J. Electrochem. Soc. **156**, A283 (2009)
102. T.D. Hatchard, J.R. Dahn, J. Electrochem. Soc. **151**, A838 (2004)
103. T.D. Hatchard, M.N. Obrovac, J.R. Dahn, J. Electrochem. Soc. **153**, A282 (2006)
104. P. Ge, M. Fouletier, Solid State Ionics **28–30**, 1172 (1988)
105. J. Sangster, C.W. Bale, J. Phase Equilib. Diffus. **19**, 76 (1998)
106. Z. Du, R.A. Dunlap, M.N. Obrovac, J. Alloys Compd. **617**, 271 (2014)
107. L. Baggetto, P. Ganesh, R.P. Meisner, R.R. Unocic, J.C. Jumas, C.A. Bridges, G.M. Veith, J. Power Sources **234**, 48 (2013)
108. S. Komaba, Y. Matsuura, T. Ishikawa, N. Yabuuchi, W. Murata, S. Kuze, Electrochem. Commun. **21**, 65 (2012)
109. L.D. Ellis, T.D. Hatchard, M.N. Obrovac, J. Electrochem. Soc. **159**, A1801 (2012)
110. J.W. Wang, X.H. Liu, S.X. Mao, J.Y. Huang, Nano Lett. **12**, 5897 (2012)
111. J.M. Stratford et al., J. Am. Chem. Soc. **139**, 7273 (2017)
112. R. Benedek, M.M. Thackeray, J. Power Sources **110**, 406 (2002)
113. M. Winter, J.O. Besenhard, Electrochim. Acta **45**, 31 (1999)
114. M. Wachtler, J.O. Besenhard, M. Winter, J. Power Sources **94**, 189 (2001)
115. C.M. Ionica, L. Aldon, P.E. Lippens, F. Morato, J. Olivier-Fourcade, J.C. Jumas, Hyperfine Interact. **156**, 555 (2004)
116. Z. Du, R.A. Dunlap, M.N. Obrovac, J. Electrochem. Soc. **163**, A2011 (2016)
117. Z. Du, S.N. Ellis, R.A. Dunlap, M.N. Obrovac, J. Electrochem. Soc. **163**, A13 (2016)
118. J. Hassoun, S. Panero, G. Mulas, B. Scrosati, J. Power Sources **171**, 928 (2007)
119. O. Mao, R.A. Dunlap, J.R. Dahn, J. Electrochem. Soc. **146**, 405 (1999)
120. P.P. Ferguson, A.D.W. Todd, J.R. Dahn, Electrochem. Commun. **10**, 25 (2008)
121. P.P. Ferguson, M.L. Martine, A.E. George, J.R. Dahn, J. Power Sources **194**, 794 (2009)
122. P.P. Ferguson, M. Rajora, R.A. Dunlap, J.R. Dahn, J. Electrochem. Soc. **156**, A204 (2009)
123. F.J. Nacimiento, P. Lavela, J.L. Tirado, J.M. Jiménez, D. Barreda, R. Santamaría, Mater. Chem. Phys. **138**, 747 (2013)
124. P.P. Ferguson, R.A. Dunlap, J.R. Dahn, J. Electrochem. Soc. **157**, A326 (2010)
125. G. Venturini, B. Malaman, G. Le Caër, D. Fruchart, Phys. Rev. B **35**, 7038 (1987)
126. M. Chamas, P.E. Lippens, J.C. Jumas, K. Boukerma, R. Dedryvere, D. Gonbeau, J. Hassoun, S. Panero, B. Scrosati, J. Power Sources **196**, 7011 (2011)
127. G.L. Caer, B. Malaman, G. Venturini, D. Fruchart, B. Roques, J. Phys. F: Met. Phys. **15**, 1813 (1985)
128. U.G. Nwokeke, R. Alcántara, J.L. Tirado, R. Stoyanova, M. Yoncheva, E. Zhecheva, Chem. Mater. **22**, 2268 (2010)

129. A. Mahmoud, M. Chamas, J.-C. Jumas, B. Philippe, R. Dedryvere, D. Gonbeau, I. Saadoune, P.E. Lippens, J. Power Sources **244**, 246 (2013)
130. B. Philippe, A. Mahmoud, J.B. Ledeuil, M.T. Sougrati, K. Edstrom, R. Dedryvere, D. Gonbeau, P.E. Lippens, Electrochim. Acta **123**, 72 (2014)
131. F. Nacimiento, R. Alcántara, J.L. Tirado, J. Electrochem. Soc. **157**, A666 (2010)
132. S. Wang, M. He, M. Walter, F. Krumeich, K.V. Kravchyk, M.V. Kovalenko, Nanoscale **10**, 6827 (2018)
133. K.K.D. Ehinon, S. Naille, R. Dedryvere, P.E. Lippens, J.C. Jumas, D. Gonbeau, Chem. Mater. **20**, 5388 (2008)
134. S. Naille, R. Dedryvere, D. Zitoun, P.E. Lippens, J. Power Sources **189**, 806 (2009)
135. S. Naille, P.E. Lippens, F. Morato, J. Olivier-Fourcade, Hyperfine Interact. **167**, 785 (2006)
136. S. Naille, R. Dedryvere, H. Martinez, S. Leroy, P.E. Lippens, J.C. Jumas, D. Gonbeau, J. Power Sources **174**, 1086 (2007)
137. L. Fransson, E. Nordström, K. Edström, L. Häggström, J.T. Vaughey, M.M. Thackeray, J. Electrochem. Soc. **149**, A736 (2002)
138. J. Wolfenstine, S. Campos, D. Foster, J. Read, W.K. Behl, J. Power Sources **109**, 230 (2002)
139. X.F. Tan, S.D. McDonald, Q. Gu, Y. Hu, L. Wang, S. Matsumura, T. Nishimura, K. Nogita, J. Power Sources **415**, 50 (2019)
140. G. Le Caer, B. Malaman, G. Venturini, I. B. Kim, Phys. Rev. B **26**, 5085 (1982)
141. S. Naille, C.M. Ionica-Bousquet, F. Robert, F. Morato, P.E. Lippens, J. Olivier-Fourcade, J. Power Sources **174**, 1091 (2007)
142. S. Furuseth, H. Fjellvag, Acta Chem. Scand. A **40** (1986)
143. T. Azib, N. Bibent, M. Latroche, F. Fischer, J.-C. Jumas, J. Olivier-Fourcade, C. Jordy, P. E. Lippens, F. Cuevas, J. Mater. Chem. A **8**, 18132 (2020)
144. Z. Edfouf, F. Cuevas, M. Latroche, C. Georges, C. Jordy, T. Hézèque, G. Caillon, J.C. Jumas, M.T. Sougrati, J. Power Sources **196**, 4762 (2011)
145. Z. Edfouf, C. Fariaut-Georges, F. Cuevas, M. Latroche, T. Hézèque, G. Caillon, C. Jordy, M.T. Sougrati, J.C. Jumas, Electrochim. Acta **89**, 365 (2013)
146. M. Broussely, P. Biensan, F. Bonhomme, P. Blanchard, S. Herreyre, K. Nechev, R.J. Staniewicz, J. Power Sources **146**, 90 (2005)
147. M. Chamas, A. Mahmoud, J. Tang, M.T. Sougrati, S. Panero, P.E. Lippens, J. Phys. Chem. C **121**, 217 (2017)
148. J. Chouvin, J. Olivier-Fourcade, J.C. Jumas, B. Simon, P. Biensan, F.J. Fernández Madrigal, J.L. Tirado, C. Pérez Vicente, J. Electroanal. Chem. **494**, 136 (2000)
149. I.A. Courtney, R.A. Dunlap, J.R. Dahn, Electrochim. Acta **45**, 51 (1999)
150. I. Sandu, T. Brousse, J. Santos-Peña, M. Danot, D.M. Schleich, Ionics **8**, 27 (2002)